An improved global-direction stencil based on the face-area-weighted centroid for the gradient reconstruction of unstructured finite volume methods[*]

Ling-Fa Kong(孔令发)[1], Yi-Dao Dong(董义道)[1,†], Wei Liu(刘伟)[1], and Huai-Bao Zhang(张怀宝)[2]

[1]*College of Aerospace Science and Engineering, National University of Defense Technology, Changsha 410073, China*
[2]*School of Physics, Sun Yat-sen University, Guangzhou 510275, China*

The accuracy of unstructured finite volume methods is greatly influenced by the gradient reconstruction, for which the stencil selection plays a critical role. Compared with the commonly used face-neighbor and vertex-neighbor stencils, the global-direction stencil is independent of the mesh topology, and characteristics of the flow field can be well reflected by this novel stencil. However, for a high-aspect-ratio triangular grid, the grid skewness is evident, which is one of the most important grid-quality measures known to affect the accuracy and stability of finite volume solvers. On this basis and inspired by an approach of using face-area-weighted centroid to reduce the grid skewness, we explore a method by combining the global-direction stencil and face-area-weighted centroid on high-aspect-ratio triangular grids, so as to improve the computational accuracy. Four representative numerical cases are simulated on high-aspect-ratio triangular grids to examine the validity of the improved global-direction stencil. Results illustrate that errors of this improved methods are the lowest among all methods we tested, and in high-mach-number flow, with the increase of cell aspect ratio, the improved global-direction stencil always has a better stability than commonly used face-neighbor and vertex-neighbor stencils. Therefore, the computational accuracy as well as stability is greatly improved, and superiorities of this novel method are verified.

Keywords: unstructured finite volume methods, improved global-direction stencil, grid skewness, face-area-weighted centroid

PACS: 02.60.Cb, 47.11.–j, 47.11.Df   **DOI:** 10.1088/1674-1056/aba2da

1. Introduction

Unstructured grids are commonly used in simulation of computational fluid dynamics (CFD).[1] Compared with the structured grid,[2] this kind of grids is easy to generate without heavily manual intervention, and has a better adaptability to different engineering shapes.[3–6] Therefore, compared with the block-structured grid, utilizing unstructured grid brings a lot of flexibilities.[7] Nowadays, the most widely used algorithms for unstructured grids are second-order finite volume methods (FVM)[8–10] adopted by many well-known software packages, such as Ansys's fluent (http://www.ansys.com) and the open source software OpenFOAM (http://openfoam.org), and the accuracy of these algorithms is greatly influenced by the gradient reconstruction, for which the stencil selection plays a critical role. One commonly used stencil selection method selects cells that share faces with the central cell. For this method, the stencil size equals the number of cell faces and we name it as face-neighbor stencil. Sometimes, vertex-adjacent cells that share vertices with the central cell are also included to construct the stencil and we name it as vertex-neighbor stencil. This method contains much more stencil cells, while it is almost impossible to obtain a constant stencil size.

Apart from the methods mentioned above, Xiong *et al.*[11]

proposed a stencil selection method in 2018 and named it as the local-direction stencil selection method, where stencil cells are augmented along two local directions. In this method, characteristics of flow fields are taken into account during the process of determining local directions, and one of them is close to the boundary normal vector. However, when grid cells have high aspect ratio, the cells selected by this method may deviate a lot from the boundary normal. In addition, the implementation process of this method is very complicated. Compared with the local-direction stencil selection method, the global-direction stencil selection method is well performed. In this method, instead of using different local directions, for each cell, two global directions, that is, normal and tangential directions of the wall, are employed for all cells within the computational domain. Stencil cells selected by this novel global-direction stencil selection method are always along the normal and tangential directions of the wall, even on high-aspect-ratio triangular grids.

For some typical flows, global-direction stencil cells can well reflect flow-field characteristics and capture the variation of flow variables, such as the boundary-layer-type flow. However, after analysis, the only data required for the gradient reconstruction are not stencil cells themselves, but flow variables evaluated at the reference point within grid cells. Usu-

†Corresponding author. E-mail: tianyatingxiao@163.com
http://iopscience.iop.org/cpb   http://cpb.iphy.ac.cn

ally, the geometric centroid is chosen as the reference point. Hence, although stencil cells selected by the global-direction stencil selection method are along the normal and tangential directions of the wall, it is difficult to determine whether the variation of the flow field can be accurately captured by the reference points within stencil cells or not, especially for high-aspect-ratio triangular grids, because this kind of grids is highly anisotropic and easily skewed, that is, connections of geometric centroids along the normal direction are obviously deflective. In this sense, the original motivation of capturing the flow-field gradient by a global-direction stencil is violated on cells with high aspect ratio. Therefore, in order to achieve a better reflection of flow-field characteristics on highly anisotropic grids, reducing grid skewness is one of the feasible ways.

The grid skewness is one of the most important grid-quality measures known to affect the stability and computational accuracy of CFD solvers.[5,12–17] There are various definitions of the grid skewness, such as the angle between face normal and the vector pointing from the face centroid to the cell centroid,[18] the minimal internal angle of grid cell,[19] and the ratio of the max diagonal to the minimum.[15] Apart from these definitions, there is a typical definition closely related to the finite volume discretization.[20] It is defined at a face shared by two neighbor cells, say, A and B, as the dot product of the unit vector pointing from the centroid of cell A to that of cell B, and the unit face normal vector pointing from cell A to B.[20] Thus a non-skewed grid has the measure 1 and a highly-skewed grid nearly 0. From the definition, we can clearly find if we want to reduce the grid skewness, we can only redesign a grid without high aspect ratio to achieve the skewness reduction. However, for some typical flows, such as the boundary-layer-type flow, cells close to the wall are always required to be set with high aspect ratio, due to the large normal gradient of flow variables. Therefore, highly anisotropic grid cannot be avoided, and we can only rely on a new "centroid" inside of the grid cell to replace the geometric centroid for the skewness reduction.

Usually, unstructured finite volume methods (FVM) are constructed based on the integral form, where solution and source term vectors are treated as the cell-averaged values. However, for second-order finite volume methods, cell-averaged values can be evaluated as the point value at the geometric centroid,[7–9] which is named as the reference point. Using the geometric centroid brings a lot of advantages, for example, the average value of solution and source term vectors can be easily performed by one-point quadrature, which is second-order accurate for linear functions.[21–23] In 2016 Sejekan et al.[24] proposed a new reference point named as the containment center, which is defined as the center of the smallest circle that can enclose a given triangle. The use of this new reference point instead provides better stability, and

the designed order of accuracy is achieved. Apart from the integral form, in Ref. [20], Nishikawa illustrated that the same finite volume methods can be constructed based on the differential form, where solution and source term vectors are not cell-averaged values but point-values, which are evaluated at the reference point. Furthermore, Nishikawa proved that the finite volume method with differential form can also maintain the second-order accuracy without source term integration, and the reference point can be located anywhere within a grid cell.[20] More importantly, this conclusion sets the stage for the grid skewness reduction.

Given the freedom to choose the reference point, for a simplex-element grid[25] (i.e., a triangular grid in two dimensions), which is widely used in the simulation of boundary layers, it can be easily skewed, especially on high-aspect-ratio triangular grids. Nishikawa[20] proposed a new "centroid" and named it as the face-area-weighted centroid. By face-area-weighted formula, the connection of new reference points is almost parallel to the boundary normal vector, and the grid skewness is obviously reduced. On this basis, some improvements are proposed in this paper, where the finite volume method constructed by the differential form is employed, and solution as well as source term vectors are evaluated as point-values at the reference point. In addition, the global-direction stencil cells are combined with the face-area-weighted centroid[20] to obtain the skewness reduction on high-aspect-ratio triangular cells and a more accurate reflection of the flow-field characteristics. Finally, four representative numerical cases will be utilized to examine the computational accuracy and stability of this improved global-direction stencil, and we compare the results with stencils using the geometric centroid, including vertex-neighbor and face-neighbor stencils, as well as the global-direction stencil.

The structure of this paper is organized as follows. In Section 2, the governing equations with integral and differential forms, as well as spatial discretization, are described. The improved global-direction stencil with the face-area-weighted centroid are presented in Section 3. Moreover, two commonly used face-neighbor and vertex-neighbor stencil selection methods, as well as the local-direction and global-direction stencil selection methods are reviewed and analyzed in this section. In Section 4, four numerical examples with the straight or curved boundary are presented to preliminarily verify the effectiveness of this improvement. Conclusions and future work will be summarized in Section 5.

2. Unstructured finite volume methods

In this section, the discretization of second-order finite volume methods from integral form is given firstly. For the integral form, both solution and source term vectors are cell-averaged values. Furthermore, the differential form of finite

volume methods, where the solution and source term vectors are treated as point-values at the reference point, is also demonstrated.

2.1. Finite volume method from integral form

The integral governing equation for the inviscid problem can be written as

$$\iint_V \frac{\partial \boldsymbol{u}}{\partial t}\,\mathrm{d}V + \iint_V \nabla \cdot \boldsymbol{F}\,\mathrm{d}V = \iint_V \boldsymbol{s}\,\mathrm{d}V, \tag{1}$$

where $\boldsymbol{u}$ is a solution vector, V is a control volume, and $\boldsymbol{s}$ is a source term vector. For the inviscid problem, $\boldsymbol{F}$ denotes the convective flux tensor with the form of

$$\boldsymbol{F} = \begin{pmatrix} \rho \boldsymbol{v} \\ \rho \boldsymbol{v} \otimes \boldsymbol{v} + p\boldsymbol{I} \\ \rho \boldsymbol{v} H \end{pmatrix}, \tag{2}$$

where ρ is the density, $\boldsymbol{v}$ is the velocity vector, p is the pressure, H is the specific total enthalpy,

$$H = \left[\gamma P/(\gamma - 1) + \rho v^2/2 \right]/\rho, \tag{3}$$

and $\otimes$ represents the dyadic product of two vectors. Equation (1) can be transformed by Gauss formula as

$$\iint_V \frac{\partial \boldsymbol{u}}{\partial t}\,\mathrm{d}V + \oint_{\partial V} \boldsymbol{F}_\mathrm{n}\,\mathrm{d}S = \iint_V \boldsymbol{s}\,\mathrm{d}V, \tag{4}$$

where ∂V denotes the boundary of control volume, $\boldsymbol{F}_\mathrm{n}$ is the flux along the outward normal vector of cell faces. With the second-order discretization, the semi-discrete scheme can be formulated as

$$\frac{\mathrm{d}\bar{\boldsymbol{u}}_i}{\mathrm{d}t} + \frac{1}{V_i} \sum_{m=1}^{N_f} \boldsymbol{\Phi}_{im} S_{im} = \frac{1}{V_i} \iint_{V_i} \boldsymbol{s}\,\mathrm{d}V, \tag{5}$$

where $\bar{\boldsymbol{u}}_i$ is the cell-averaged value of the solution vector,

$$\bar{\boldsymbol{u}}_i = \frac{1}{V_i} \iint_{V_i} \boldsymbol{u}_i \mathrm{d}V. \tag{6}$$

For the second-order finite volume method, $\bar{\boldsymbol{u}}$ is always replaced by the point value that is evaluated at the cell centroid. In addition, N_f is the number of cell faces, S_m is the face area, and $\boldsymbol{\Phi}_{im}$ is the numerical flux computed at the face centroid.
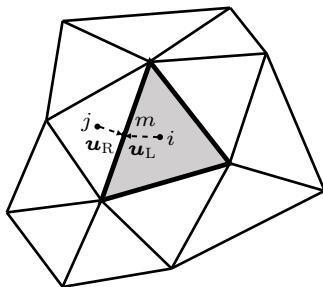

Fig. 1. The process of cell-centered finite volume discretization on triangular cells.

As shown in Fig. 1, to compute the numerical flux with approximate Riemann solvers,[26] left and right state vectors need to be calculated,

$$\begin{cases} \boldsymbol{u}_\mathrm{L}^\mathrm{n} = \bar{\boldsymbol{u}}_i + \nabla \boldsymbol{u}_i \cdot (\boldsymbol{x}_m - \boldsymbol{x}_i), \\ \boldsymbol{u}_\mathrm{R}^\mathrm{n} = \bar{\boldsymbol{u}}_j + \nabla \boldsymbol{u}_j \cdot (\boldsymbol{x}_m - \boldsymbol{x}_j), \end{cases} \tag{7}$$

where $\nabla \boldsymbol{u}_i$ and $\nabla \boldsymbol{u}_j$ represent the solution gradients of cell i and cell j, respectively; $\boldsymbol{x}_m$ is face centroid; $\boldsymbol{x}_i$ and $\boldsymbol{x}_j$ are reference points of two cells. In this paper, the least square (LSQR) method[27] will be employed for the gradient reconstruction, and the process will be given in Section 2.3. Moreover, the Roe scheme[28] is utilized to compute the numerical flux,

$$\begin{aligned} \boldsymbol{\Phi}_{im} = {} & \frac{1}{2}\left[\boldsymbol{F}_\mathrm{n}(\boldsymbol{u}_\mathrm{L}^\mathrm{n}) + \boldsymbol{F}_\mathrm{n}(\boldsymbol{u}_\mathrm{R}^\mathrm{n}) \right] \\ & - \frac{1}{2}\left| \bar{\boldsymbol{A}}(\boldsymbol{u}_\mathrm{L}^\mathrm{n}, \boldsymbol{u}_\mathrm{R}^\mathrm{n}) \right| (\boldsymbol{u}_\mathrm{L}^\mathrm{n} - \boldsymbol{u}_\mathrm{R}^\mathrm{n}), \end{aligned} \tag{8}$$

where $\bar{\boldsymbol{A}}(\boldsymbol{u}_\mathrm{L}^\mathrm{n}, \boldsymbol{u}_\mathrm{R}^\mathrm{n})$ denotes the Jacobian coefficient matrix linearized by the Roe average method.[28]

For the second-order finite volume method, source term is always calculated by one-point quadrature at the reference point. Hence, Eq. (5) can be written as

$$\frac{\mathrm{d}\bar{\boldsymbol{u}}_i}{\mathrm{d}t} + \frac{1}{V_i} \sum_{m=1}^{N_\mathrm{f}} \boldsymbol{\Phi}_{im} S_{im} = \boldsymbol{s}_i, \tag{9}$$

where $\boldsymbol{s}_i$ is the source term vector evaluated at the reference point. As mentioned above, the reference point is always chosen at the geometric centroid. If it is chosen anywhere, the final result will not be second-order accurate for linear function, unless the source term is a constant.

2.2. Finite volume method from differential form

Apart from the integral form mentioned in Section 2.1, in this paper, the finite volume method with the differential form is employed, and the governing equation is

$$\frac{\mathrm{d}\boldsymbol{u}_i}{\mathrm{d}t} + \nabla \cdot \boldsymbol{F} = \boldsymbol{s}_i. \tag{10}$$

As Eq. (2) demonstrated, the flux is a linear function, and therefore, the flux divergence can be transformed into

$$\nabla \cdot \boldsymbol{F} = \frac{1}{V_i} \iint_{V_i} \nabla \cdot \boldsymbol{F}\,\mathrm{d}V = \oint_{\partial V_i} \boldsymbol{F}_\mathrm{n}\,\mathrm{d}S. \tag{11}$$

Hence, Eq. (10) can be written as

$$\frac{\mathrm{d}\boldsymbol{u}_i}{\mathrm{d}t} + \frac{1}{V_i} \oint_{\partial V_i} \boldsymbol{F}_\mathrm{n}\,\mathrm{d}S = \boldsymbol{s}_i, \tag{12}$$

where flux integration can be solved by the numerical quadrature,

$$\frac{\mathrm{d}\boldsymbol{u}_i}{\mathrm{d}t} + \frac{1}{V_i} \sum_{m=1}^{N_\mathrm{f}} \boldsymbol{\Phi}_{im} S_{im} = \boldsymbol{s}_i. \tag{13}$$

In Eq. (13), both u_i and s_i are treated as point-values and evaluated at the reference point, and numerical flux $\boldsymbol{\Phi}_{im}$ is also constructed by the Roe scheme.[28] For differential finite volume methods, the reference point can be located anywhere within the grid cell, and the second-order accuracy will always be kept. On this basis, apart from the geometric centroid, a better reference point that is beneficial to the numerical performance of the FVM solver can be employed on stencil cells.

2.3. The least square gradient reconstruction

The evaluation of solution gradient by the least square (LSQR) method was first introduced by Barth and Jespersen.[27] The LSQR method is based on the Taylor expansion of variable u_k at the reference point within the k-th stencil cell. In order to get an optimal approximation, a least-square-error function to reflect the sum of truncation errors within stencil cells is computed for the central cell i,

$$E_i = \sum_{k=1}^{N_{\mathrm{s}}} \left\{ \omega_k \left[u_k - \left(u_i + \nabla u_i \cdot \boldsymbol{r}_{i,k} + o(h) \right) \right]^2 \right\}, \quad (14)$$

where N_{s} is the number of stencil cells, u_k is the exact value of solution within the k-th stencil cell, and $u_i + \nabla u_i \cdot \boldsymbol{r}_{i,k} + o(h)$ is the first-order-accurate Taylar series approximation for cell k with $o(h)$ being infinitely small, where $\boldsymbol{r}_{i,k}$ denotes the vector pointing from the reference point of cell i to that of cell k. In order to reflect the influence degree of different stencil cells, the weight ω_k is defined as

$$\omega_k = \frac{1}{|\boldsymbol{r}_{i,k}|}, \quad (15)$$

which is set to emphasize the data geometrically close to the central cell. For the two-dimensional unstructured grid, Eq. (14) can be written as

$$E_i = \sum_{k=1}^{N_{\mathrm{s}}} \left\{ \omega_k \left[\Delta u_{k,i} - \Delta x_{i,k} \left(\frac{\partial u}{\partial x} \right)_i - \Delta y_{i,k} \left(\frac{\partial u}{\partial y} \right)_i \right]^2 \right\}, \quad (16)$$

where $\Delta u_{k,i} = u_i - u_k$, $\Delta x_{i,k} = \boldsymbol{r}_{i,k} \cdot \boldsymbol{i}$ and $\Delta y_{i,k} = \boldsymbol{r}_{i,k} \cdot \boldsymbol{j}$. In order to derive the coefficients of different stencil cells, Eq. (16) can be formulated as

$$\begin{cases} \dfrac{\partial E_i}{\partial \left(\frac{\partial u}{\partial x} \right)_i} = \displaystyle\sum_{k=1}^{N_{\mathrm{s}}} 2\omega_k \Delta x_{i,k} \left[\Delta u_{k,i} - \Delta x_{i,k} \left(\frac{\partial u}{\partial x} \right)_i - \Delta y_{i,k} \left(\frac{\partial u}{\partial y} \right)_i \right], \\[4mm] \dfrac{\partial E_i}{\partial \left(\frac{\partial u}{\partial y} \right)_i} = \displaystyle\sum_{k=1}^{N_{\mathrm{s}}} 2\omega_k \Delta y_{i,k} \left[\Delta u_{k,i} - \Delta x_{i,k} \left(\frac{\partial u}{\partial x} \right)_i - \Delta y_{i,k} \left(\frac{\partial u}{\partial y} \right)_i \right]. \end{cases} \quad (17)$$

This equation is utilized to get the minimum value of truncation errors. When truncation errors reach the minimum, we have two derivatives $\partial E_i / \partial \left(\frac{\partial u}{\partial x} \right)_i = 0$ and $\partial E_i / \partial \left(\frac{\partial u}{\partial y} \right)_i = 0$, i.e., solution of the k-th stencil cell can be accurately reconstructed by that of cell i with the second-order accuracy. Therefore, we only need to solve the equation shown as follows:

$$\begin{cases} 0 = \displaystyle\sum_{k=1}^{N_{\mathrm{s}}} \left[2\omega_k \Delta x_{i,k} \Delta u_{k,i} - 2\omega_k \Delta x_{i,k}^2 \left(\frac{\partial u}{\partial x} \right)_i - 2\omega_k \Delta x_{i,k} \Delta y_{i,k} \left(\frac{\partial u}{\partial y} \right)_i \right], \\[4mm] 0 = \displaystyle\sum_{k=1}^{N_{\mathrm{s}}} \left[2\omega_k \Delta y_{i,k} \Delta u_{k,i} - 2\omega_k \Delta y_{i,k} \Delta x_{i,k} \left(\frac{\partial u}{\partial x} \right)_i - 2\omega_k \Delta y_{i,k}^2 \left(\frac{\partial u}{\partial y} \right)_i \right]. \end{cases} \quad (18)$$

A linear system of equations can be constructed to solve Eq. (18),

$$\begin{pmatrix} \sum\limits_{k=1}^{N_{\mathrm{s}}} \omega_k \Delta x_{i,k}^2 & \sum\limits_{k=1}^{N_{\mathrm{s}}} \omega_k \Delta x_{i,k} \Delta y_{i,k} \\ \sum\limits_{k=1}^{N_{\mathrm{s}}} \omega_k \Delta y_{i,k} \Delta x_{i,k} & \sum\limits_{k=1}^{N_{\mathrm{s}}} \omega_k \Delta y_{i,k}^2 \end{pmatrix} \begin{pmatrix} \dfrac{\partial u}{\partial x} \\ \dfrac{\partial u}{\partial y} \end{pmatrix}_i = \begin{pmatrix} \sum\limits_{k=1}^{N_{\mathrm{s}}} \omega_k \Delta x_{i,k} \Delta u_{i,k} \\ \sum\limits_{k=1}^{N_{\mathrm{s}}} \omega_k \Delta y_{i,k} \Delta u_{i,k} \end{pmatrix}. \quad (19)$$

Once the gradients of cell i are obtained, two state vectors can be computed as Eq. (7), and the numerical flux will be calculated. In addition, as mentioned above, there is another important factor affecting the gradient reconstruction, that is, the stencil selection method, and in the next section, we will focus on different stencils.

3. Stencil selection methods

In this section, the global-direction stencil selection method and two commonly used face-neighbor and vertex-neighbor stencil selection methods, as well as the local-direction stencil selection method,[11] are reviewed and analyzed firstly. Then, the optimization of global-direction stencil selection method for grids with the curved boundary is performed. In adition, to achieve a better reflection of the flow field, combination of the face-area-weighted centroid and global-direction stencil will be given in Section 3.2.

3.1. Review and analysis of commonly used and global-direction stencil selection methods

Commonly used stencils are face-neighbor and vertex-neighbor stencils. As shown in Fig. 2, the face-neighbor stencil includes entire neighbor cells that share faces with the central cell, and the vertex-neighbor stencil is constructed by neighbor cells that share vertices with the central cell. Both face-neighbor and vertex-neighbor stencils are dependent on the fixed mesh topology. As a result, characteristics of the flow field are not well reflected.
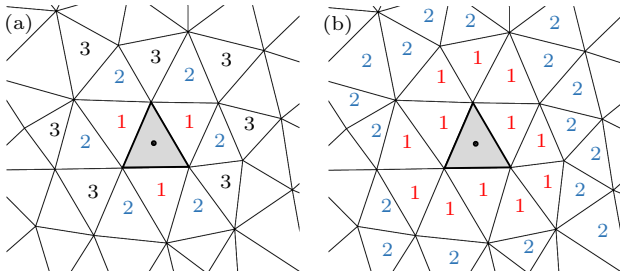
Fig. 2. Face-neighbor and vertex-neighbor stencil cells in different layers. The different numbers in these two figures represent the diverse stencil layers (e.g., for vertex-neighbor stencil, the first layer stencil is composed of all cells that share vertices with the central cell, and the second layer stencil consists of cells that share vertices with the first layer stencil). (a) Face-neighbor stencil. (b) Vertex-neighbor stencil.
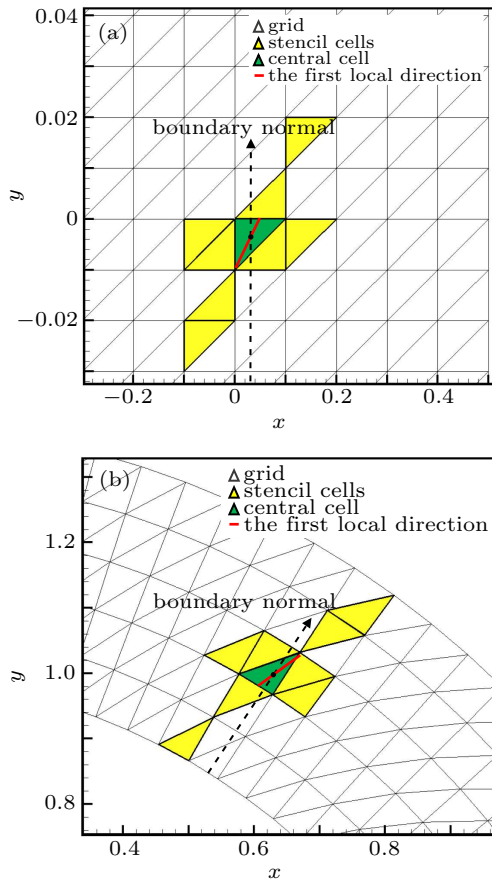
Fig. 3. Local direction stencils on triangular grids with minor aspect ratio. (a) Grid with straight boundary. (b) Grid with curved boundary.

Apart from two commonly used stencil selection methods, in 2018, Xiong *et al.*[11] put forward a stencil selection

method based on local directions, by which they imitated characteristics of the structured grid and capture the variation of flow field.

As shown in Fig. 3, all stencil cells are along two local directions, demonstrating the structured characteristic, and close to normal and tangential directions of the wall. For some typical flows such as the boundary layer type flow, variables along the boundary normal direction are changed dramatically. Hence, this variation can be effectively captured by local-direction stencil cells.

Usually, cells in a boundary layer are set with high aspect ratio to improve the resolution ratio. From Fig. 4, we can easily find if the grid has high aspect ratio, one of the local directions has severely deviated from the normal direction of the wall, resulting in the poor reflection of the flow-field characteristics. The implementation process of this method is very complicated.
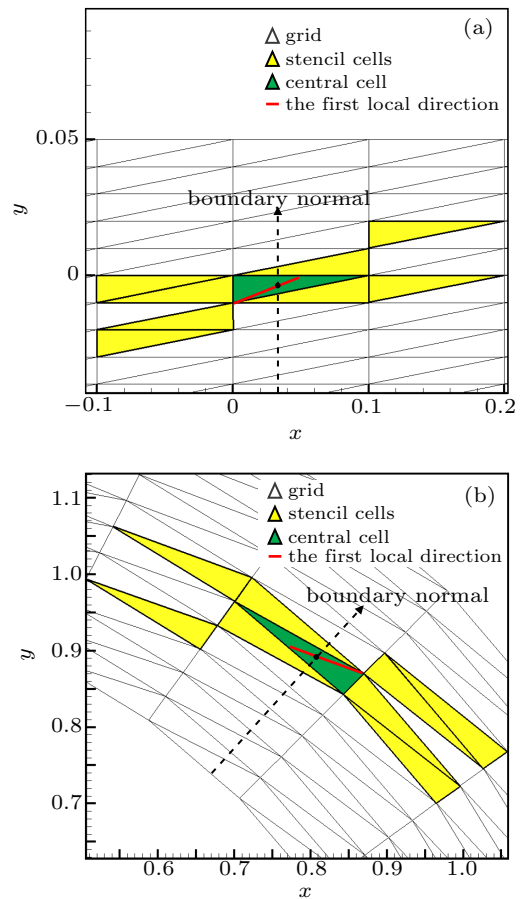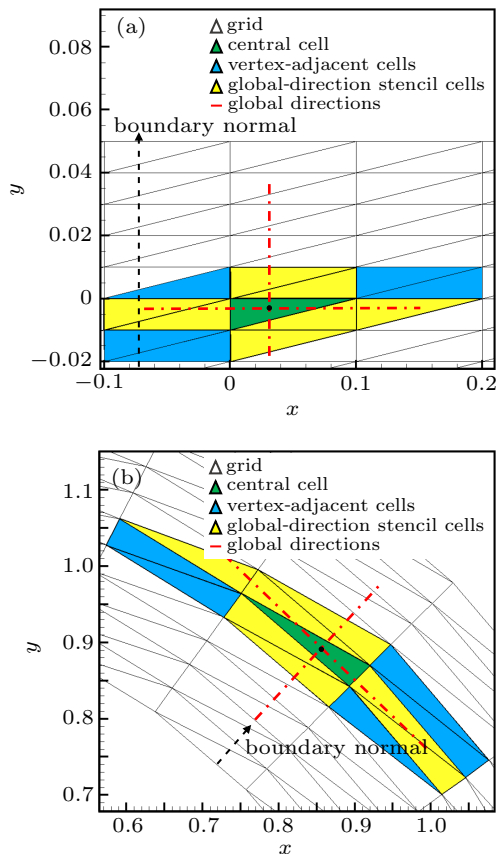

Fig. 4. Local direction stencils on triangular grids with high aspect ratio. (a) Grid with straight boundary. (b) Grid with curved boundary.

Compared with local-direction stencil, the global-direction stencil selection method overcomes the problems mentioned above, and has a better adaptability to high-aspect-ratio triangular grids. For this method, two global directions are determined firstly. One is along the normal direction of the wall, and to achieve a better spatial ductility, the other one is along the wall tangential. Then, for each central cell, two lines

that are parallel to global directions respectively and pass the cell centroid are generated. Finally, cells in a given set, such as the vertex-neighbor cells that intersect with these two lines, are selected to construct the new stencil.

For simple-shape cases, two global directions can be easily determined. However, for problems with irregular or complex surface, there is no analytic function to compute the normal vector of the wall. In this situation, we can refer to the method of computing wall distance at the reference point to obtain the normal vector.[29] On this basis, for problems with complex surface, two global directions can also be obtained.

However, it should be noted that grid cells are not always consistent with the flow anisotropy, especially in parallel computing. In this situation, the stencil selection of the whole computational domain could be divided into two parts. The global-direction stencil selection method can be utilized for cells adjacent to the wall surface, because flow anisotropy is quite evident at this local field. Some commonly used stencil selection methods, for example, the face-neighbor and vertex-neighbor methods, could be employed on other fields.

As shown in Fig. 5, on high-aspect-ratio triangular grids with straight and curved boundary, global-direction stencil cells are always along normal and tangential directions of the wall. Therefore, the flow anisotropy can be well reflected, and the manipulation of this novel stencil selection method is more concise and convenient, compared with that of the local-direction stencil selection method.

However, some problems of this novel stencil selection method are found later on grids with the curved boundary and higher aspect ratio, that is, with the increase of cell aspect ratio, wrong cells will be selected along the tangential direction of the wall. After analysis, the reason is concluded. For this kind of grids, there are too small spacing in the radial direction and large spacing in the circumferential direction, and stencil cells along the stream-wise direction are selected only by a line parallel to the tangential direction of the wall, which will definitely result in redundant or even insufficient cells to be selected.

For internal cells, this phenomenon will lead to excess cells to be selected, whereas for boundary-adjacent cells, the number of selected stencil cells will not be enough to solve the equations of gradient reconstruction.
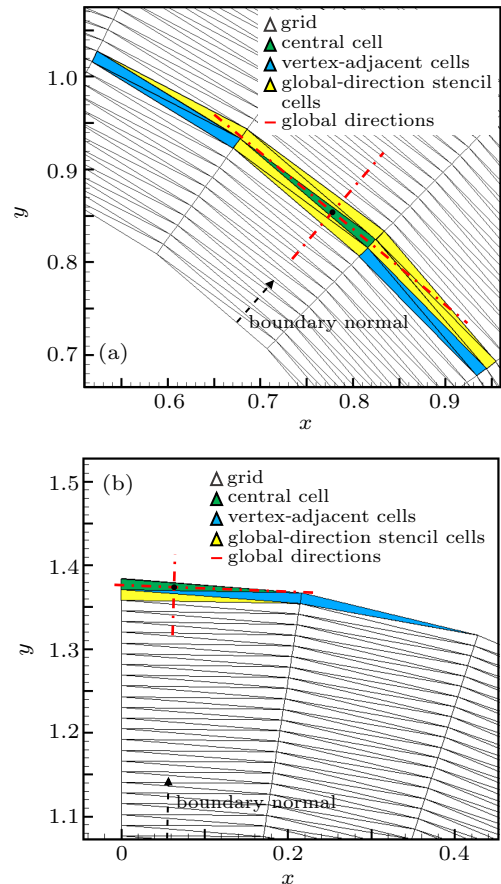
Fig. 5. The global-direction stencils on triangular girds with high aspect ratio. (a) Grid with straight boundary. (b) Grid with curved boundary.

Fig. 6. Global-direction stencils at internal field and the curved boundary on high-aspect-ratio triangular grids. (a) Internal field. (b) Curved boundary.

On this basis, the implementation process is greatly simplified, and flow anisotropy in the boundary layer can also be well reflected by the corresponding global-direction stencil cells.

As shown in Fig. 6(b), for this central cell, only one stencil cell is selected, but for the second-order accurate gradi-

ent reconstruction, as Eq. (19) demonstrated, there are two unknowns need to be solved, and therefore, the optimization need to be performed for the global-direction stencil selection method on grids with the curved boundary and high aspect ratio. Stencil cells along the normal direction of the wall can be selected directly, but cells along the tangential direction of the wall need to be adjusted to guarantee them are along the stream-wise direction.

As shown in Fig. 7, after optimization, global-direction stencil cells on grids with the curved boundary are always along the wall normal and stream-wise directions no matter how high aspect ratio of grid cells is. Hence, shortcomings on grids with the curved boundary and high aspect ratio are effectively eliminated.
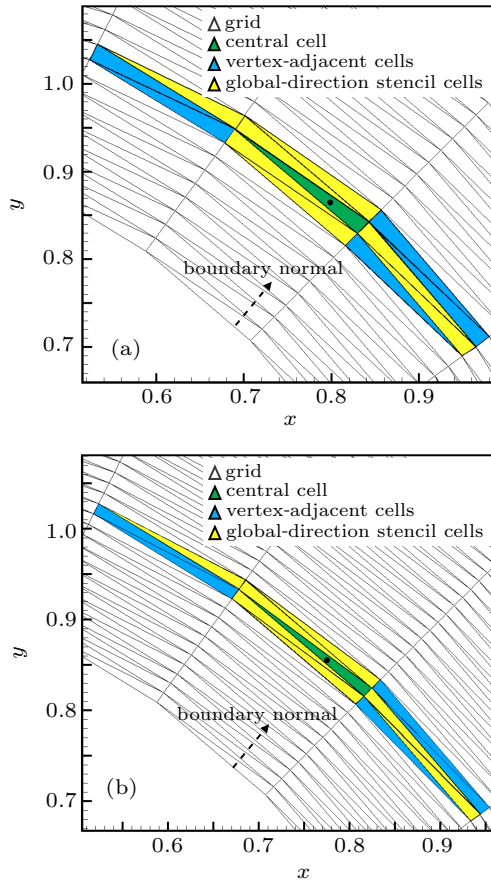
Fig. 7. The optimized global-direction stencil cells on grids with the curved boundary and high aspect ratio. (a) Grid 1. (b) Grid 2.

3.2. Improved global-direction stencil based on the face-area-weighted centroid

In this section, the face-area-weighted centroid[20] is analyzed firstly, and a typical high-aspect-ratio triangular grid is utilized to analytically discuss the skewness reduction by the employment of this novel reference point. The improvement about the combination of global-direction stencil and face-area-weighted centroid will also be demonstrated in detail.

3.2.1. Face-area-weighted centroid of triangular cell

For simplex-element grids,[25] the face-area-weighted centroid is proposed in Ref. [20] to replace the geometric centroid. As shown in Fig. 8(a), connection of the geometric centroids exhibits the serrated characteristic. This phenomenon is adverse to the accuracy and stability of the FVM solver. However, as shown in Fig. 8(b), lines connecting the face-area-weighted centroids are almost parallel to the normal direction of the wall.
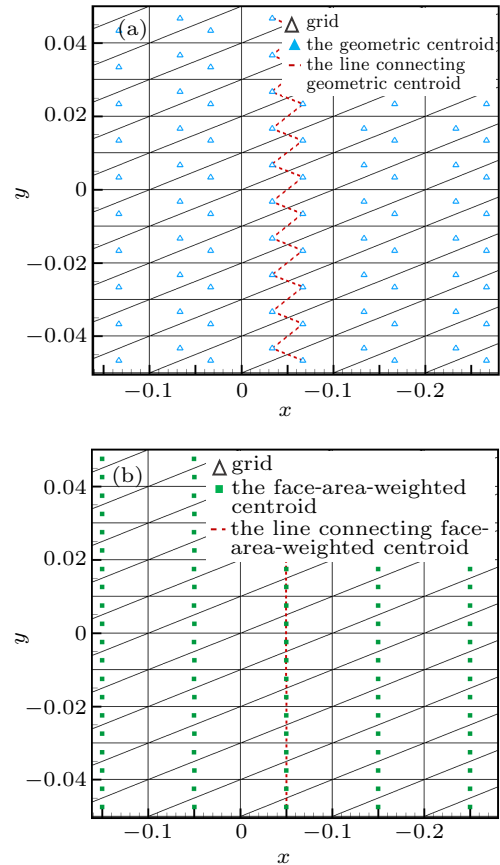

Fig. 8. The geometric centroid and face-area-weighted centroid of triangular cells. (a) Geometric centroid. (b) Face-area-weighted centroid.

Compared with the geometric centroid, use of face-area-weighted centroid effectively reduces the grid skewness, and the measure is demonstrated in Fig. 9.
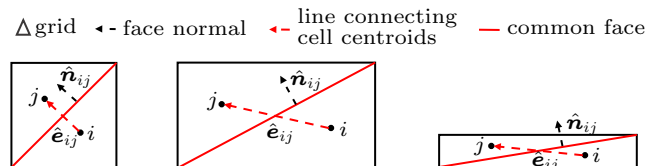

Fig. 9. The grid skewness measure of cells in different aspect ratios.

In Fig. 9, the grid skewness measure is defined at a common face shared by two neighbor cells, say, i and j, where $\hat{e}_{ij}$ is the unit vector along the connection of two cell centroids, $\hat{n}_{ij}$ denotes the outward unit normal vector of this common

face, and the measure of grid skewness is defined as the dot product of two unit vectors, that is, the non-skewed grid with $\hat{e}_{ij} \cdot \hat{n}_{ij} = 1$ and highly skewed grid with $\hat{e}_{ij} \cdot \hat{n}_{ij} = 0$.

From Fig. 9, we find that with the increase of cell aspect ratio, the angle between two unit vectors $\hat{e}_{ij}$ and $\hat{n}_{ij}$ increases at the same time, and therefore, the grid is gradually skewed. For some typical flows, boundary-adjacent cells are often set with high aspect ratio to capture the variation of flow variables. As a result, if the geometric centroid is still chosen as the reference point, high grid skewness cannot be avoided. In the following, the conclusion of grid skewness measure on simplex-element grid[25] will be summarized.

For two-dimensional triangular grids, cell centroid can be expressed by the arithmetic average of the face centroids (midpoints in 2D)

$$(x_j, y_j) = \frac{1}{3} \sum_{k=1}^{3} (x_{mk}, y_{mk}), \tag{20}$$

where (x_{mk}, y_{mk}) is coordinate of the k-th face centroid. The face-area-weighted centroid[20] can be written as

$$(x_j, y_j) = \frac{\sum\limits_{k=1}^{3} \hat{A}_{jk}^{p}(x_{mk}, y_{mk})}{\sum\limits_{k=1}^{3} \hat{A}_{jk}^{p}},$$

$$\hat{A}_{jk} = \frac{A_{jk}}{\max\limits_{k \in \{1,2,3\}} A_{jk}}, \tag{21}$$

where A_{jk} represents the area (length) of common faces across cell j and k, and p (> 0) is a parameter to control the degree of grid skewness.

Consider a typical regular triangular grid as shown in Fig. 10. Here R denotes the cell aspect ratio, and h is the spacing in y-direction. As $R \to \infty$, the skewness measure approaches 1 at the vertical face, but can become arbitrarily small for other faces: e.g., faces between cells 1 and 2, cells 2 and 3.
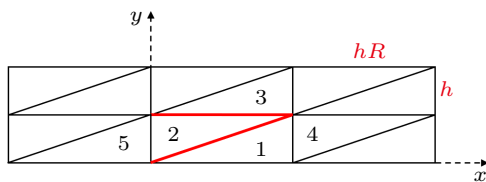

Fig. 10. A typical high-aspect-ratio triangular grid in Cartesian-coordinate system.

It is verified in Ref. [20] that with the increase of p, the grid skewness will decrease dramatically on high-aspect-ratio triangular grids. When $p = 2$, the measure of grid skewness reaches 1 between cells 1 and 2, cells 2 and 3. Therefore, the grid skewness can be totally eliminated by the employment of face-area-weighted centroid in different p values.
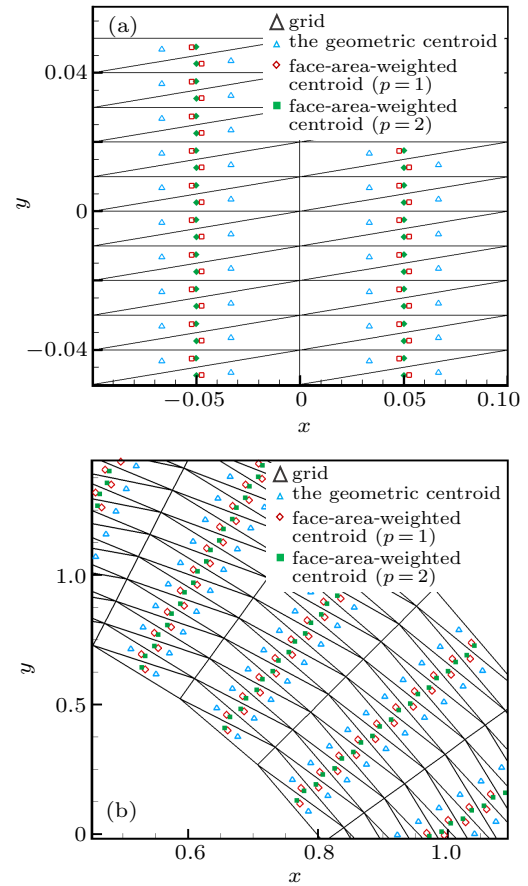

Fig. 11. The geometric centroid and face-area-weighted centroid with different parameter p on grids with straight and curved boundary respectively. (a) Grid with straight boundary. (b) Grid with curved boundary.

As shown in Fig. 11, compared with the geometric centroid, the grid skewness can be effectively reduced by the employment of face-area-weighted centroid. With the increase of parameter p, connections of face-area-weighted centroid are closer to the normal direction of the wall, regardless of the grid with straight or curved boundary. This phenomenon just coincides with our original motivation of designing the global-direction stencil selection method. Inspired by that, we wonder whether the face-area-weighted centroid can be used on the global-direction stencil, to achieve a more accurate reflection of the flow-field characteristics.

3.2.2. The employment of face-area-weighted centroid on global-direction stencil

As mentioned above, characteristics of the flow field can be well reflected by global-direction stencil cells, and the manipulation of this novel stencil selection method is more concise. Cells selected by the global-direction stencil selection method are always along the normal direction of the wall and stream-wise direction regardless of the grid with high aspect ratio or not.

After analysis, though global-direction stencil cells are along the normal and tangential directions of the wall, the only data required for the gradient reconstruction are flow vari-

ables evaluated at the reference point, rather than stencil cells themselves. Therefore, the location of reference point within the stencil cell is more decisive. As mentioned above, lines connecting the geometric centroids are highly skewed, especially on high-aspect-ratio triangular grids, but the connection of face-area-weighted centroids is almost parallel to the normal direction of the wall.

On this basis, in order to reduce the grid skewness and to reflect flow field characteristics more accurately, we attempt to improve the global-direction stencil by combining the face-area-weighted centroid with globald-direction stencil cells.
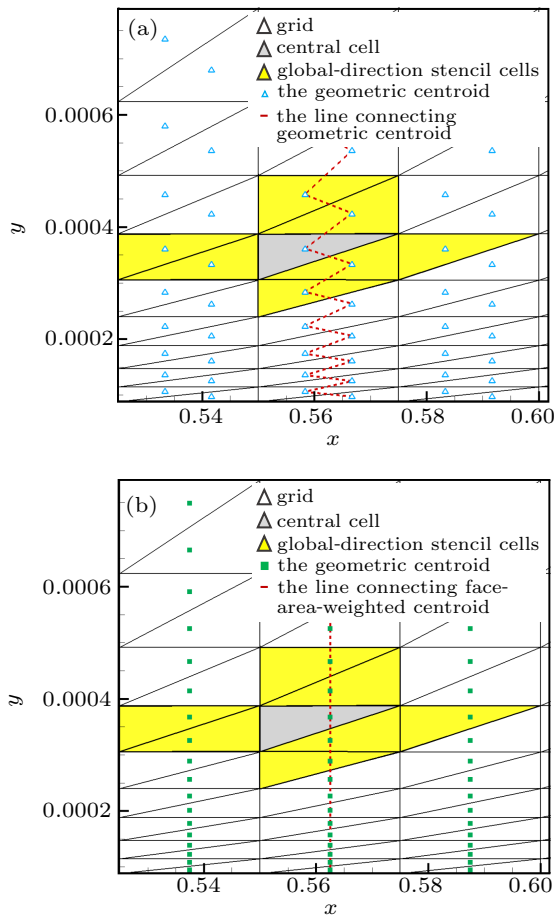
Fig. 12. The global-direction stencils combined with geometric centroid and face-area-weighted centroid on regular triangular grid used for the boundary layer type flow. (a) Geometric centroid. (b) Face-area-weighted centroid.

As shown in Figs. 12 and 13, we can find that the line connecting face-area-weighted centroids is closer to the normal direction of the wall than that of geometric centroids, no matter whether they are on grids with the curved boundary or not. As a result, the improved global-direction stencil has a better reflection of the flow-field variation than original global-direction stencil with the geometric centroid.
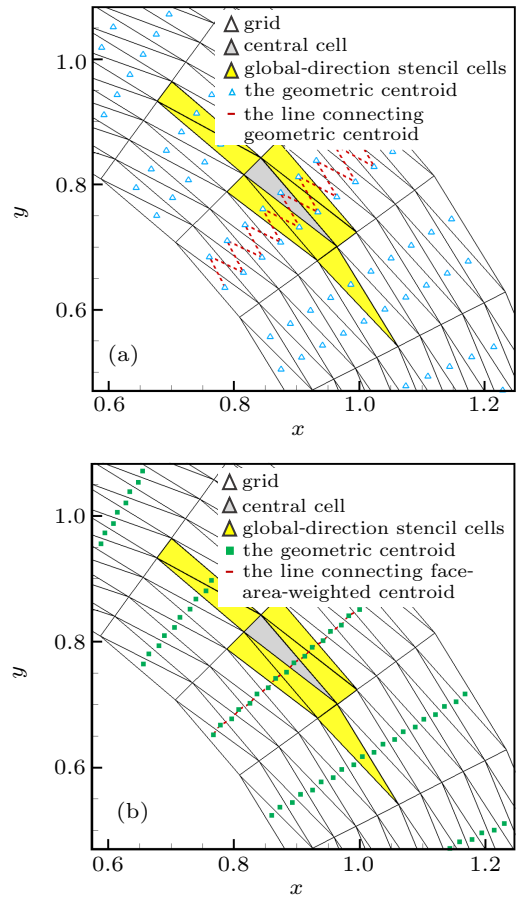
Fig. 13. The global-direction stencils combined with geometric centroid and face-area-weighted centroid on triangular grid with the curved boundary. (a) Geometric centroid. (b) Face-area-weighted centroid.

4. Numerical examples

To verify the effectiveness of the improved global-direction stencil, four representative numerical examples are employed. In Sections 4.1 and 4.2, the method of manufactured solutions (MMS)[30–33] is employed on Euler equations to simulate boundary-layer type flow and verify the accuracy for different stencil selection methods. In Section 4.3, supersonic vortex flow is introduced to test the validity of this improved global-direction stencil on grids with the curved boundary. Finally, double mach reflection of strong shock waves is simulated in Section 4.4 to further examine the numerical performance of different methods on flow with high mach number.

For comparison, these four numerical examples are simulated with five different stencils, including the improved global-direction stencils with $p = 1$ and 2, and three stencils with the geometric centroid including the commonly used vertex-neighbor and face-neighbor stencils, as well as the global-direction stencil. For the sake of simplifying the presentation in the following analysis, different stencils are abbreviated as listed in Table 1.

**Table 1.** The abbreviation of different stencils.

Full name	Abbreviation
Vertex-neighbor stencil	V-stencil
Face-neighbor stencil	F-stencil
Global-direction stencil with geometric centroid (i.e., $p = 0$)	G-stencil ($p = 0$)
Global-direction stencil with the face-area-weighted centroid and $p = 1$	G-stencil ($p = 1$)
Global-direction stencil with the face-area-weighted centroid and $p = 2$	G-stencil ($p = 2$)

4.1. The case of Euler equations with the manufactured solutions

In this section, to verify the second-order accuracy with the point-value evaluation of solution and source term vectors, the Euler equations are employed with the form of Eq. (12), and the analytic solutions[20] are as follows:

$$
\begin{cases}
\rho = 1.12 + 0.15 \sin\left[\pi\left(3.12x + 1895.92y\right)\right], \\
u = 1.32 + 0.06 \sin\left[\pi\left(2.09x + 2099.21y\right)\right], \\
v = 1.18 + 0.03 \sin\left[\pi\left(2.15x + 2001.32y\right)\right], \\
p = 1.62 + 0.31 \sin\left[\pi\left(3.79x + 1973.98y\right)\right],
\end{cases}
\tag{22}
$$

and the flow fields of this numerical example is shown in Fig. 14.
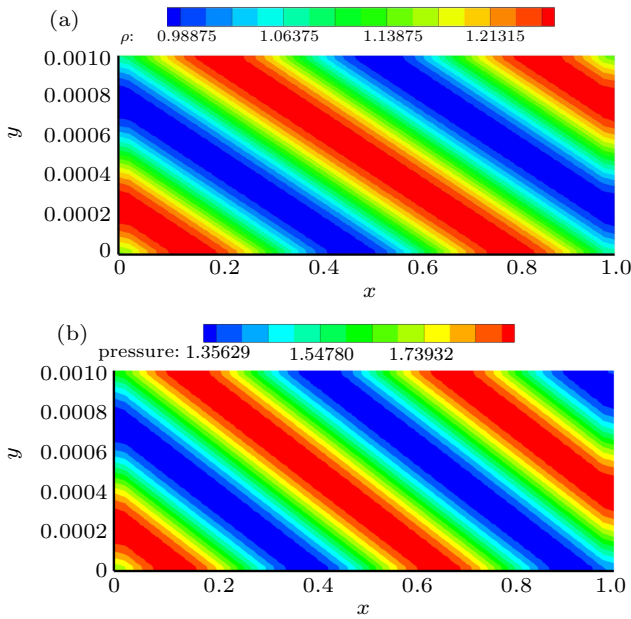
Fig. 14. Flow fields of this numerical example. (a) Density. (b) Pressure.

The source term vector can be computed from the above analytic solutions and their derivatives as

$$
s = \begin{pmatrix}
\dfrac{\partial(\rho u)}{\partial x} + \dfrac{\partial(\rho v)}{\partial y} \\[2mm]
\dfrac{\partial(\rho u^2)}{\partial x} + \dfrac{\partial(\rho uv)}{\partial y} + \dfrac{\partial p}{\partial x} \\[2mm]
\dfrac{\partial(\rho uv)}{\partial x} + \dfrac{\partial(\rho v^2)}{\partial y} + \dfrac{\partial p}{\partial y} \\[2mm]
\dfrac{\partial(\rho uH)}{\partial x} + \dfrac{\partial(\rho vH)}{\partial y}
\end{pmatrix}
$$

$$
= \begin{pmatrix}
u\dfrac{\partial\rho}{\partial x} + \rho\dfrac{\partial u}{\partial x} + v\dfrac{\partial\rho}{\partial y} + \rho\dfrac{\partial v}{\partial y} \\[2mm]
2\rho u\dfrac{\partial u}{\partial x} + u^2\dfrac{\partial\rho}{\partial x} + \rho\left(v\dfrac{\partial u}{\partial y} + u\dfrac{\partial v}{\partial y}\right) + uv\dfrac{\partial\rho}{\partial y} + \dfrac{\partial p}{\partial x} \\[2mm]
2\rho v\dfrac{\partial v}{\partial y} + v^2\dfrac{\partial\rho}{\partial y} + \rho\left(v\dfrac{\partial u}{\partial x} + u\dfrac{\partial v}{\partial x}\right) + uv\dfrac{\partial\rho}{\partial x} + \dfrac{\partial p}{\partial y} \\[2mm]
u\dfrac{\partial(\rho H)}{\partial x} + \rho H\dfrac{\partial u}{\partial x} + v\dfrac{\partial(\rho H)}{\partial y} + \rho H\dfrac{\partial v}{\partial y}
\end{pmatrix}.
\tag{23}
$$

From Eq. (22), analytic solutions $u(x,y)$ are obtained, and the numerical solutions can be computed by the FVM solver. Then, errors between analytic solutions and numerical solutions are employed as the measure of convergence accuracy. L_2 and L_∞ norms of solution errors are defined as

$$
\begin{cases}
L_2 = \sqrt{\dfrac{\sum_{i=1}^{N}\left[\left(s_i - s_{analy}\right)^2 \cdot A_i\right]}{\sum_{i=1}^{N} A_i}}, \\[3mm]
L_\infty = \max\left|s_i - s_{analy}\right|_{i=1,N},
\end{cases}
\tag{24}
$$

where s_i is the numerical solution in cell i, s_{analy} is the analytic solution, and A_i is the area of cell i. Three levels of grid aspect ratios 10^2, 5×10^2 and 10^3 are tested. In each level, five sets of regular grids in different size are generated by splitting quadrilateral grids with the right diagonals. Furthermore, the random perturbation is introduced to regular triangular grids to generate the randomly perturbed triangular grids with topology and the number of cells unchanged. Figure 15 displays regular and randomly perturbed grids with AR $= 10^3$, and the distribution of background quadrilateral grid cells from the coarsest to finest are given in Table 2.
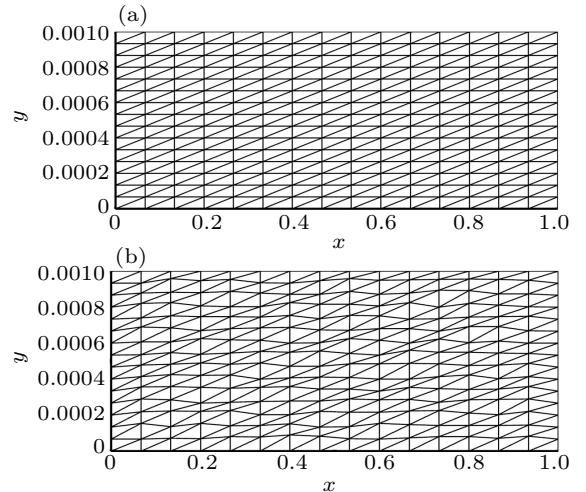

Fig. 15. Regular and randomly perturbed triangular grids with AR $=$ 10^3: (a) regular, (b) randomly perturbed.

Table 2. The distribution of five sets of background quadrilateral grid cells in different aspect ratios.

| Grid name | Distribution in x and y directions ($x, y \in [0, 1] \times [0, 0.001]$) | | |
	$AR = 10^2$	$AR = 5 \times 10^2$	$AR = 10^3$
vcoa	50×5	20×10	15×15
coa	100×10	40×20	30×30
med	150×15	60×30	45×45
fin	200×20	80×40	60×60
vfin	300×30	120×60	90×90

4.1.1. Computational results on regular triangular grids

(1) $AR = 10^2$

As shown in Fig. 16, for all of these five methods, the designed order of accuracy is achieved. For both L_2 and L_∞ pressure errors, G-stencil ($p = 0$) are always lower than that of V-stencil and L-stencil. From Fig. 17, G-stencil ($p = 0$) requires the fewest stencil cells. Hence, compared with two commonly used stencils, using G-stencil ($p = 0$) brings a better numerical performance on both computational accuracy and efficiency.
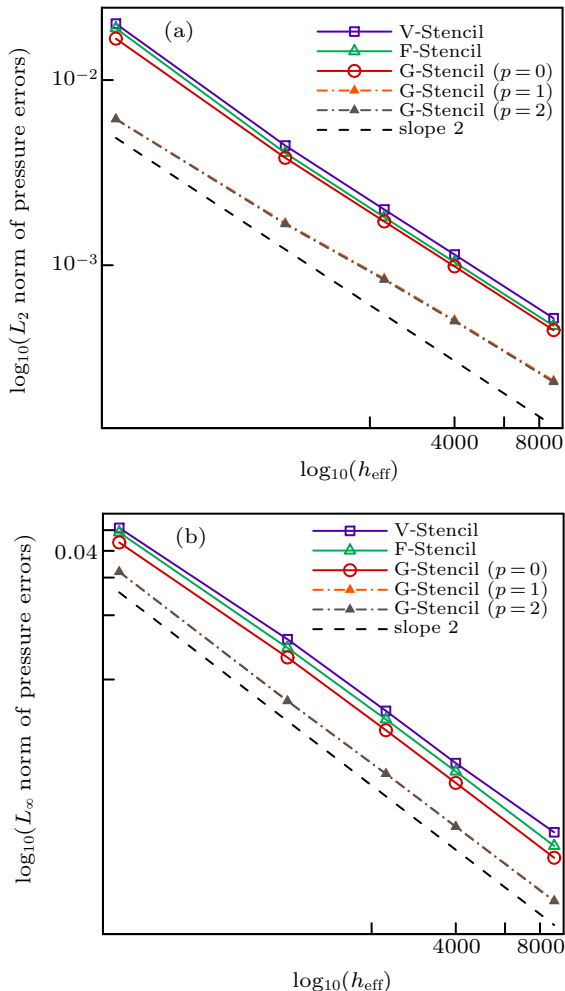
Fig. 16. L_2 and L_∞ norms of pressure errors, when the aspect ratio $AR = 10^2$: (a) L_2 norm, (b) L_∞ norm.

For the improved global-direction stencil, as shown Fig. 18, when the parameter p is higher than zero, the grid skewness is obviously reduced, and the connection of face-

area-weighted centroids is almost parallel to the normal direction of the wall. For the computational accuracy, from Fig. 16 and Table 3, we can find that errors of the improved global-direction stencil, i.e., G-stencil ($p = 1$) and G-stencil ($p = 2$), are significantly lower than those of G-stencil ($p = 0$) for both L_2 and L_∞ pressure errors. Therefore, the computational accuracy is greatly improved by this novel method.
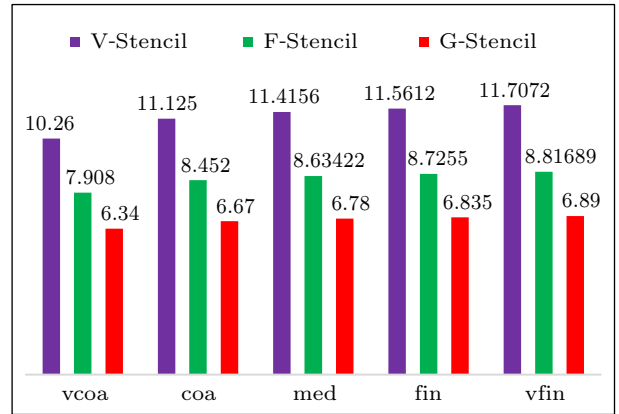

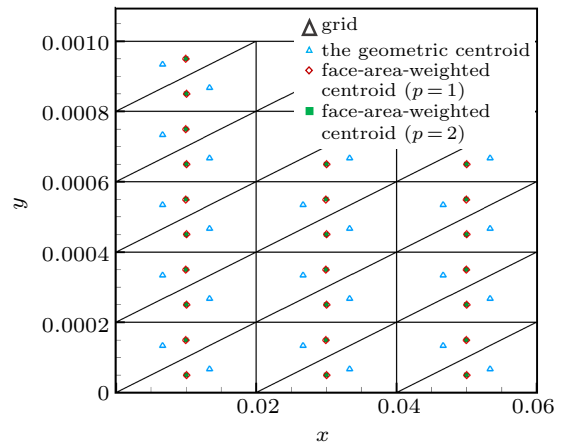**Fig. 17.** The stencil size of different stencil selection methods.

Fig. 18. The geometric centroid and face-area-weighted centroid of grid cells.

Table 3. Pressure errors of different stencils on the vfin grid.

Different stencils	L_2 norm of pressure errors	L_∞ norm of pressure errors
V-stencil	0.000517445	0.00192892
F-stencil	0.000470333	0.00166419
G-stencil ($p = 0$)	0.000446073	0.00146549
G-stencil ($p = 1$)	0.000237936	0.000923927
G-stencil ($p = 2$)	0.000234345	0.000917014

(2) $AR = 10^3$

The result of $AR = 5 \times 10^2$ is similar to that of $AR = 10^3$. Hence, in order to simplify the analysis, we only give the result of $AR = 10^3$.

As shown in Fig. 19, with the increasing cell aspect ratio, we can easily find from the results that, errors of the improved global-direction stencil are obviously lower than those of three

stencils with the geometric centroid for both L_2 and L_∞ errors. Therefore, on high-aspect-ratio triangular grids, this improved method also has a better numerical performance.
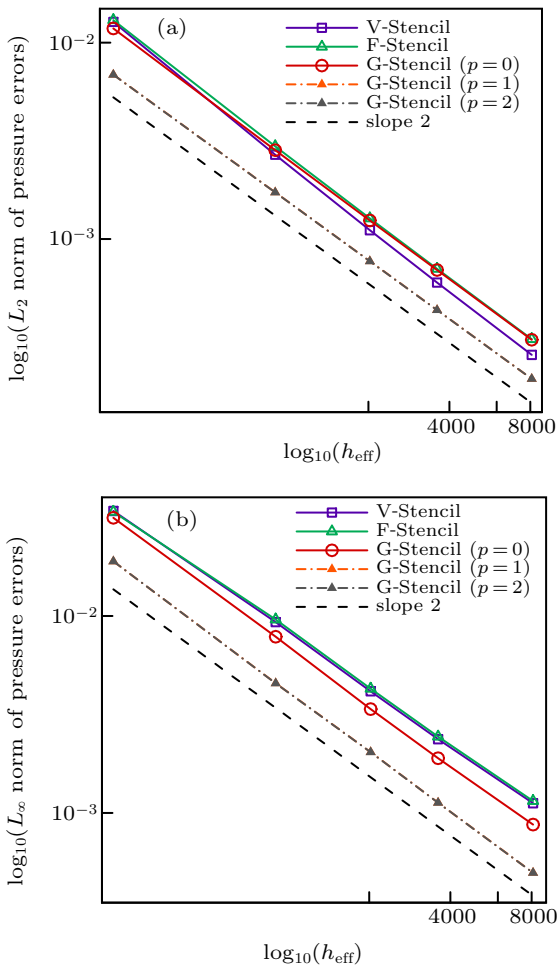

Fig. 19. L_2 and L_∞ norms of pressure errors, when the aspect ratio AR $= 10^3$: (a) L_2 norm, (b) L_∞ norm.

4.1.2. Computational results on randomly perturbed triangular grids

Perturbed grids are introduced to this numerical example, and three cases of the aspect ratio from 10^2 to 10^3 are tested. Here, results of AR $= 10^3$ are given.

It can be seen from Fig. 20 that errors on the randomly perturbed grid demonstrate the same trend to results on regular grids. For L_2 norm, errors of G-stencil ($p = 0$) are close to those of V-stencil and F-stencil, and for L_∞ norm, errors of G-stencil ($p = 0$) are always lower than those of V-stencil and F-stencil.

As shown Fig. 22, when the parameter p is higher than zero, the grid skewness is obviously reduced, and although the grid is randomly perturbed, the connection of face-area-weighted centroids is almost parallel to the normal direction of the wall. For the computational accuracy, regardless of L_2

or L_∞ norm, errors of the improved global-direction stencil are the lowest among all methods we tested. What's more, from Fig. 21, G-stencil requires the fewest stencil cells. Therefore, both the computational accuracy and efficiency are improved, and the effectiveness as well as the superiority of the improved global-direction stencil are verified on this numerical example.
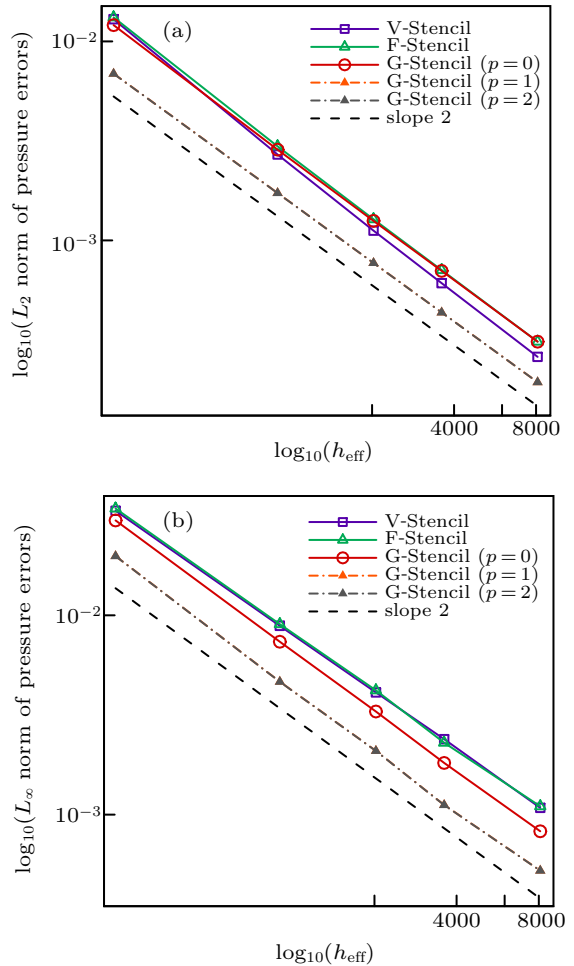

Fig. 20. L_2 and L_∞ norms of pressure errors, when the aspect ratio AR $= 10^3$: (a) L_2 norm, (b) L_∞ norm.
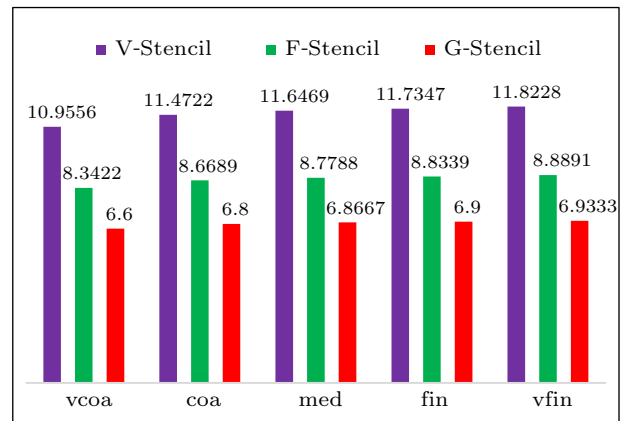

Fig. 21. The stencil size of different stencil selection methods.
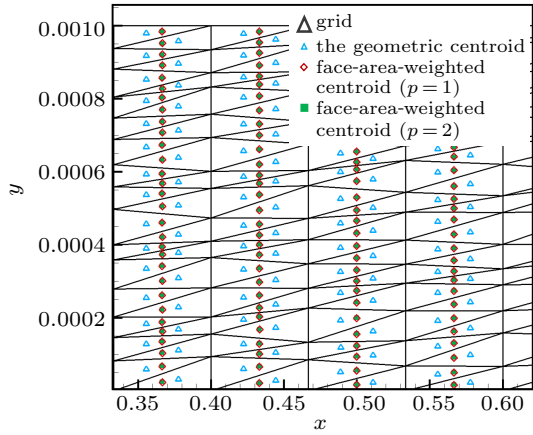
Fig. 22. The geometric centroid and face-area-weighted centroid of grid cells.

4.2. The manufactured boundary layer type flow

In this section, the method of manufactured solutions is also utilized for a scalar convective equation to simulate the boundary-layer type flow, and the manufactured solution is given as follows:

$$u(x,y) = 1 - e^{\frac{-(y-y_0)}{\sqrt{c\mu(x-x_0)}}}, \tag{25}$$

with the parameter $c = 0.59$. The parameter μ controls the thickness of the boundary layer. Flow fields corresponding to
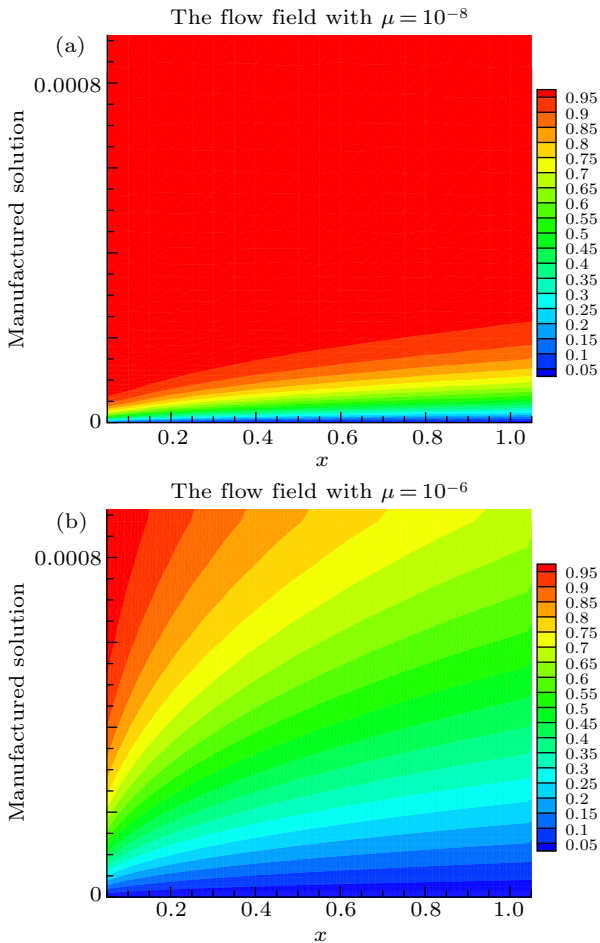
Fig. 23. The flow field of manufactured boundary layer type flow: (a) $\mu = 10^{-6}$, (b) $\mu = 10^{-8}$.

different μ values are illustrated in Fig. 23. In the following test, μ is set as 10^{-6}.

The scalar convective equation can be written as

$$\frac{\partial u}{\partial t} + \boldsymbol{a} \cdot \nabla u = 0. \tag{26}$$

With the manufactured solution substituted into Eq. (26), the modified equation with the source term can be formulated as follows:

$$\frac{\partial u}{\partial t} + \boldsymbol{a} \cdot \nabla u = \frac{a_y(y-y_0)e^{\frac{-(y-y_0)}{\sqrt{c\mu(x-x_0)}}}}{\sqrt{c\mu(x-x_0)}}$$
$$- \frac{a_x(y-y_0)e^{\frac{-(y-y_0)}{\sqrt{c\mu(x-x_0)}}}}{2\sqrt{c\mu(x-x_0)^3}}. \tag{27}$$

Therefore, the manufactured solution represents the analytical solution to the modified equation, and the numerical solution $\tilde{u}(x,y)$ can be obtained by the FVM solver. Then L_2 and L_∞ norms of errors between numerical and analytical solutions are computed with different stencils.

Both regular and randomly perturbed triangular grids, as shown in Fig. 24, are used in this example. Four levels of grid stretching are tested, including wall cell aspect-ratios (ARs) from 10^2 to 10^5. In each level, five anisotropic triangular grids with different size are generated within the computational domain($x, y \in [0.05, 1.05] \times [0, 0.001]$). During the mesh generation process, a background regular quadrilateral grid with $N = (N_x + 1) \times (N_y + 1)$ grid points and the horizontal grid spacing $h_x = 1/N_x$ is stretched in the vertical direction from $y = 0$. The y coordinates of the background grid points are defined as

$$y_{j+1} = y_j + \hat{h}_y \beta^{j+1}\big|_{j=1,2,\dots,N_y}, \tag{28}$$

where, $\hat{h}_y = h_x/\text{AR}$ is the minimal vertical grid spacing, and β is a stretching factor, which can be calculated by the known condition $y_{N_y} = 10^{-3}$. The distribution of background quadrilateral grid cells from the coarsest to finest is shown in Table 4.
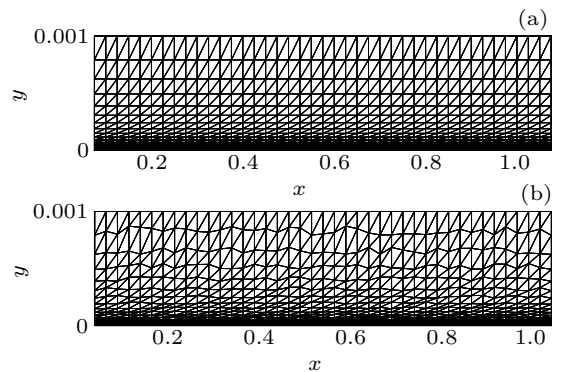

Fig. 24. Regular and randomly perturbed triangular grids with AR = 10^4: (a) regular, (b) randomly perturbed.

Table 4. The distribution of five sets of background quadrilateral grid cells in different aspect ratios.

| Grid name | Distribution in x and x directions ($x, y \in [0, 1] \times [0, 0.001]$) | | | |
	$AR = 10^2$	$AR = 10^3$	$AR = 10^4$	$AR = 10^5$
vcoa	120×10	60×20	20×30	30×30
coa	180×15	90×30	30×45	45×45
med	240×20	120×40	40×60	60×60
fin	360×30	180×60	60×90	90×90
vfin	480×40	240×80	80×120	120×120

4.2.1. Computational results on regular triangular grids

(1) $AR = 10^2$

As shown in Fig. 25, for three stencils with the geometric centroid, we can easily find that both L_2 and L_∞ errors of G-stencil ($p = 0$) are always lower than those of V-stencil and F-stencil. From Fig. 26, we find that G-stencil requires the least number of stencil cells among three different stencils. Therefore, the global-direction stencil has great superiorities on both computational accuracy and efficiency.
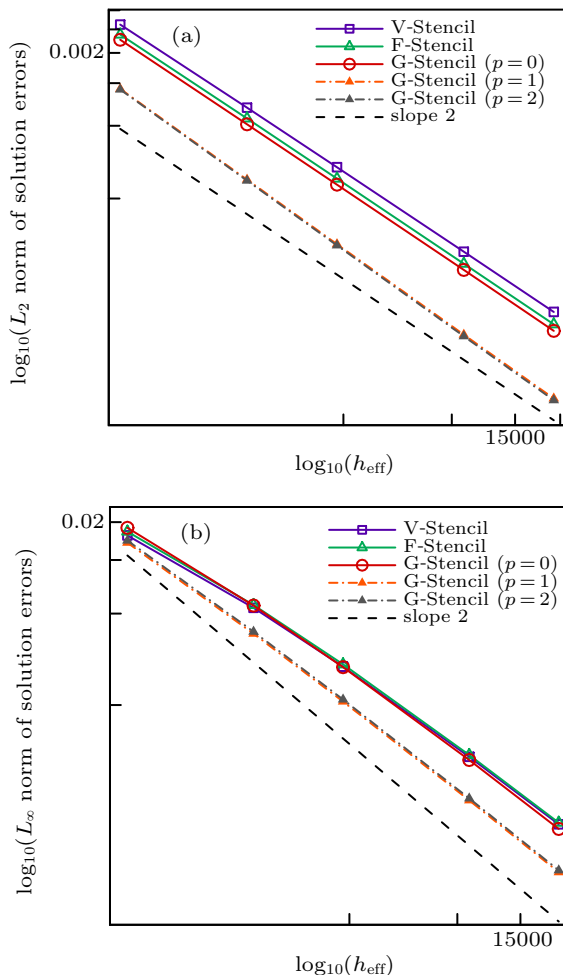
Fig. 25. L_2 and L_∞ norms of solution errors, when the aspect ratio $AR = 10^2$: (a) L_2 norm, (b) L_∞ norm.

From Fig. 27, we find when the face-area-weighted centroid is employed, the grid skewness is obviously reduced. Combined with the computational results shown in Fig. 25 and Table 5, for both L_2 and L_∞ norms, errors of the improved global-direction stencil are obviously lower than those

of V-stencil and F-stencil as well as the unimproved global-direction stencil, i.e., G-stencil ($p = 0$). As a result, the use of the face-area-weighted centroid on global-direction stencil cells greatly improves the computational accuracy.
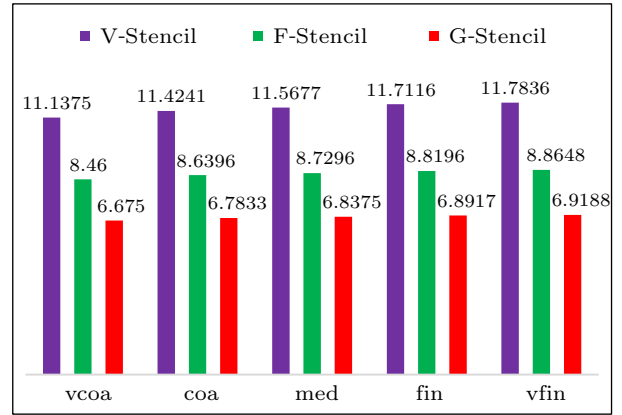

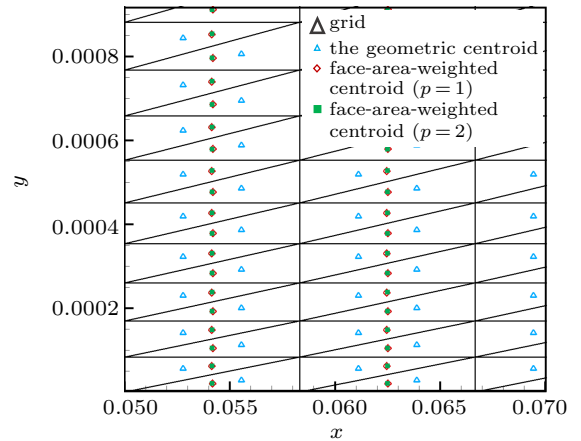**Fig. 26.** The stencil size of different stencil selection methods.

Fig. 27. The geometric centroid and face-area-weighted centroid of grid cells.

Table 5. Solution errors of different stencils on the vfin grid.

Different stencils	L_2 norm of solution errors	L_∞ norm of solution errors
V-stencil	0.000170044	0.00202639
F-stencil	0.00015098	0.00205056
G-stencil ($p = 0$)	0.00014244	0.00195697
G-stencil ($p = 1$)	0.0000746072	0.00140981
G-stencil ($p = 2$)	0.0000734274	0.00143022

(2) $AR = 10^5$

The results of $AR = 10^3$ and $AR = 10^4$ have the similar trends to that of $AR = 10^5$, and for simplicity, only the case of $AR = 10^5$ is given.

From Fig. 28, for V-stencil, F-stencil as well as G-stencil ($p = 0$), with the increase of the cell aspect ratio, L_∞ errors do not attain the second-order accuracy on finer grids. However, if the face-area-weighted centroid is employed, both L_2 and L_∞ errors reach the second-order accuracy regardless of the parameter p equaling to 1 or 2. In addition, errors of the improved global-direction stencil are significantly lower than those of three stencils with the geometric centroid. Hence, a better computational accuracy is obtained.
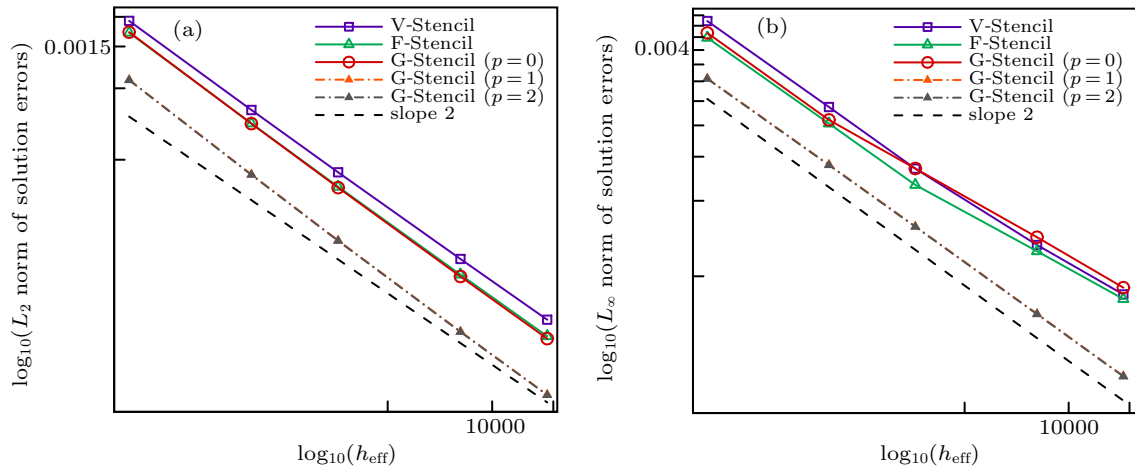
Fig. 28. L_2 and L_∞ norms of solution errors, when the aspect ratio AR $= 10^5$: (a) L_2 norm, (b) L_∞ norm.

4.2.2. Computational results on randomly perturbed triangular grids

Randomly perturbed grids are also employed in this numerical example, and the aspect ratio from 10^2 to 10^5 are tested. Here, the results of AR $= 10^4$ are given.
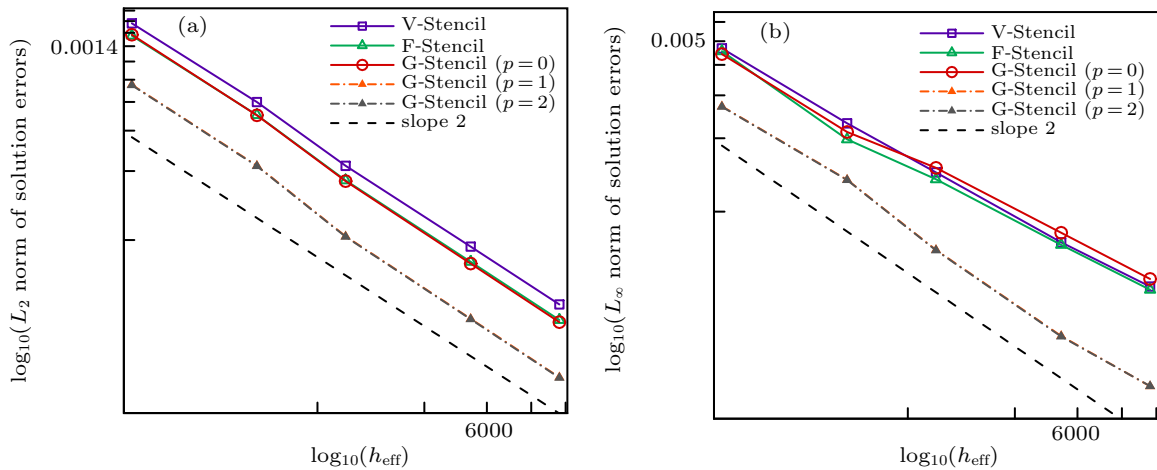

Fig. 29. L_2 and L_∞ norms of solution errors, with the aspect ratio AR $= 10^4$: (a) L_2 norm, (b) L_∞ norm.
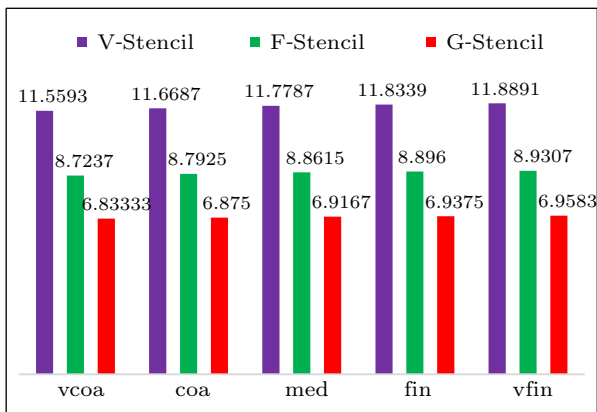
Fig. 30. The stencil size of different stencil selection methods.

rors of the improved global-direction stencil are the lowest among these five different stencils. As demonstrated by Fig. 30, G-stencil requires the fewest stencil cells. Therefore,
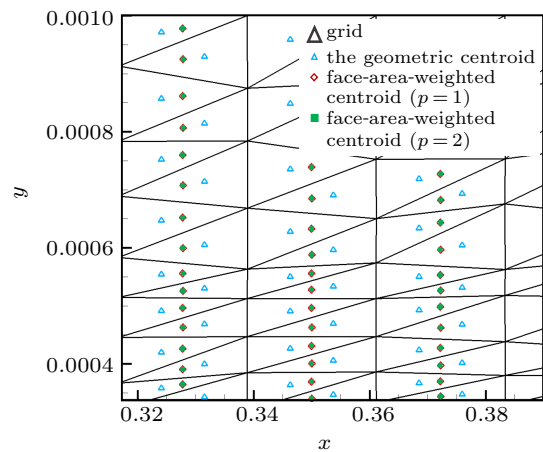

Fig. 31. The geometric centroid and face-area-weighted centroid of grid cells.

From Fig. 29, we can find that the results also give trends similar to that of a regular grid. Moreover, from Fig. 31, although the grid is randomly perturbed, grid skewness is evidently reduced by introducing the face-area-weighted centroid, and combining the results shown in Fig. 29, er-

both computational accuracy and efficiency are greatly improved, and the effectiveness as well as superiority of the improved global-direction stencil are verified on this numerical example.

4.3. Supersonic-vortex flow

In this section, the isentropic supersonic flow is simulated and analytical solution is given. The computational domain is two concentric circular arcs with radius $r_i = 1$ and $r_0 = 1.384$ located in the first quadrant. These two circular arcs represent the inviscid wall boundary, and the flow at the inlet and the outlet are supersonic. Flow fields of this numerical case are shown in Fig. 32.
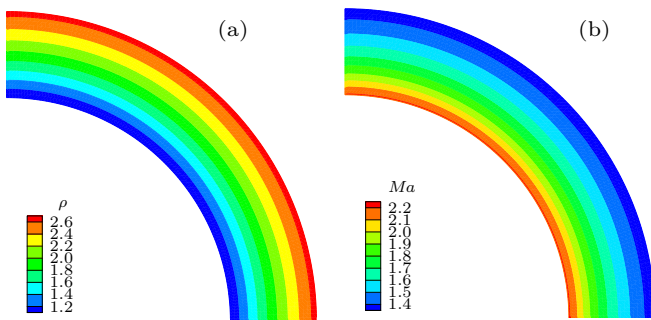

Fig. 32. Flow fields of the supersonic vortex flow: (a) density, (b) mach number.

The analytical solution of this example can be found in Refs. [34,35] and is given as follows:

$$\begin{cases} \rho = \rho_i \left[1 + \dfrac{\gamma - 1}{2} M_i^2 \left(1 - \left(\dfrac{r_i}{r} \right)^2 \right) \right]^{1/(\gamma - 1)}, \\ p = \dfrac{\rho^\gamma}{\gamma}, \\ \|\boldsymbol{v}\| = \dfrac{c_i M_i}{r}, \end{cases} \quad (29)$$

where the value of Mach number at the inner radius is $M_i = 2.25$ and the density $\rho_i = 1$. The sound speed is calculated by

$$c_i = \sqrt{\gamma \frac{p_i}{\rho_i}} = 1. \quad (30)$$

In order to fully test the numerical performance of the improved global-direction stencil, as shown in Fig. 33, regular and randomly perturbed grids are employed. The grid generation method is identical to the case in Section 4.1. For this numerical example, grids with three different aspect ratios are designed, in each level, five sets of grids ranging in different sizes are employed. Because the aspect ratios of grids with the curved boundary are not a fixed value, the wall cell aspect ratio is utilized. Three aspect ratios are approximately equal to 2.5, 4, and 8, respectively, and distributions of background quadrilateral grid cells in radial and circumferential directions on different grids are listed in Table 6.
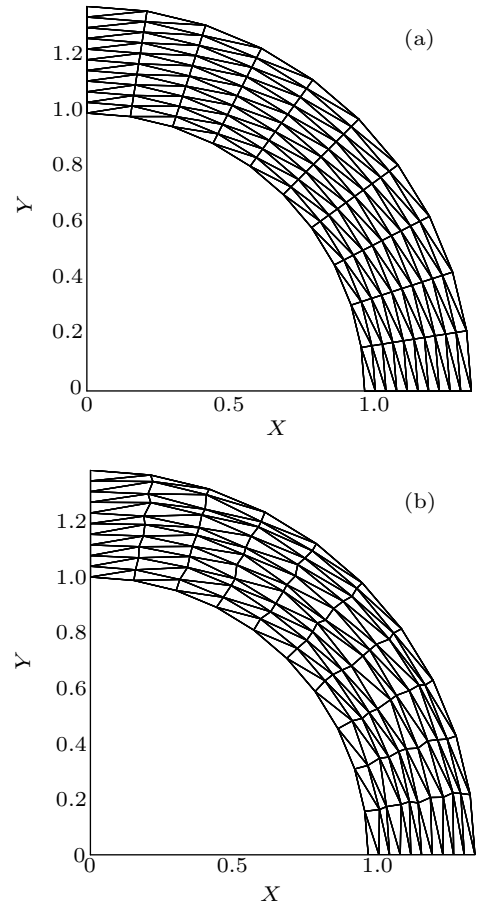

Fig. 33. Regular and randomly perturbed triangular grids with AR ≈ 4: (a) regular, (b) randomly perturbed.

Table 6. The distribution of background quadrilateral grid cells in radial and circumferential directions on three different grid categories.

Grid name	The distribution in radial and circumferential directions		
	AR ≈ 2.5	AR ≈ 4	AR ≈ 8
vcoa	20×30	10×10	20×10
coa	30×45	20×20	40×20
med	40×60	40×40	80×40
fin	60×90	60×60	120×60
vfin	80×120	80×80	160×80

Here, L_2 and L_∞ norms of global and wall pressure errors are employed as the measure of the convergence accuracy. The global errors are calculated among all cells in the computational domain, while wall errors are calculated among cells adjacent to the wall boundary.

4.3.1. Computational results on regular triangular grids

(1) AR ≈ 2.5

As shown in Fig. 35, with the increase of parameter p, the grid skewness is gradually reduced, and the connection of face-area-weighted centroids is closer to the normal direction of the wall. Moreover, combined with the computational results shown in Fig. 34 and Table 7, global pressure errors of the improved global-direction stencil are the lowest among five sencils. Therefore, the computational accuracy is greatly improved for the internal fields.
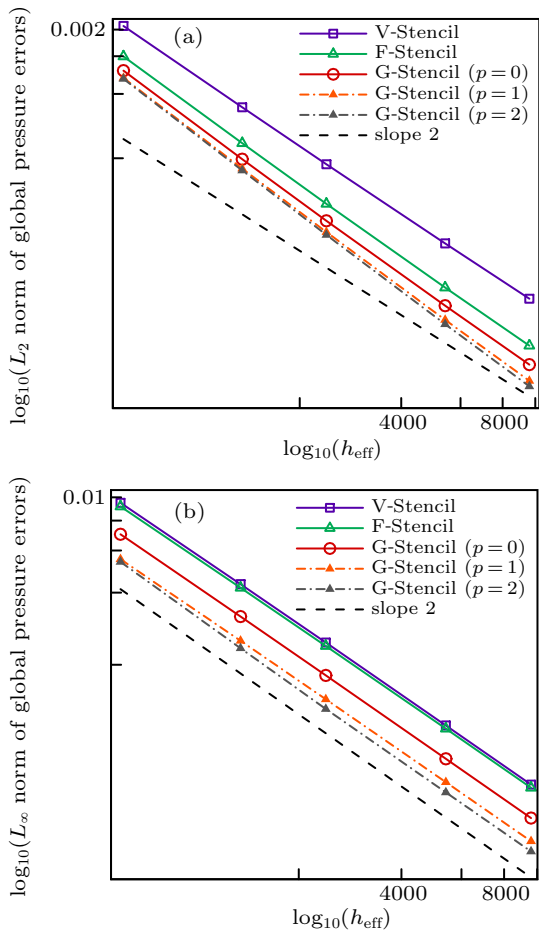
Fig. 34. L_2 and L_∞ norms of global pressure errors, and the aspect ratio AR ≈ 2.5: (a) L_2 norm, (b) L_∞ norm.

those of V-stencil and F-stencil. Moreover, errors of the improved global-direction stencil are lower than that of G-stencil ($p = 0$). Therefore, the improved global-direction stencil has a better performance not only at the internal field but also at the curved boundary.
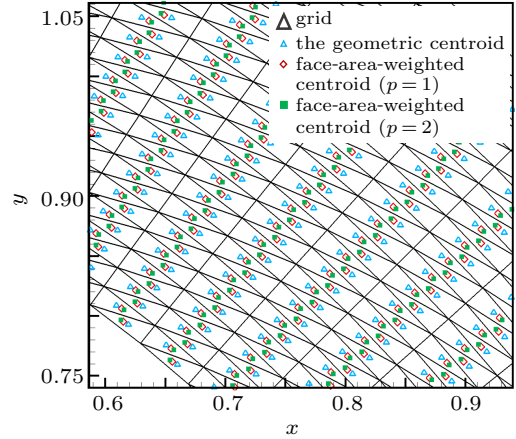

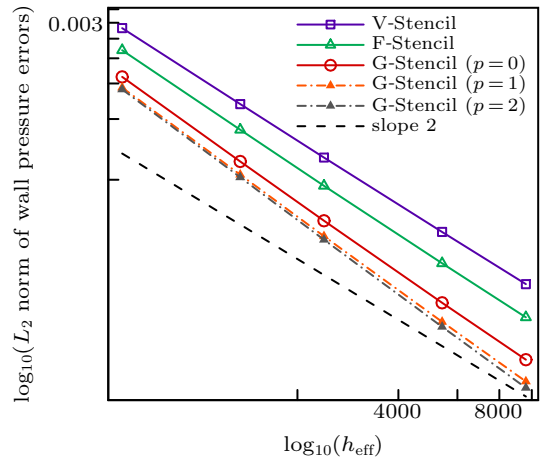**Fig. 35.** The geometric centroid and face-area-weighted centroid of grid cells.

Fig. 36. L_2 norm of wall pressure errors and the aspect ratio AR ≈ 2.5.

In order to examine the influence of the curved boundary, wall pressure errors are considered for this numerical example. Because the max value of pressure errors is located in boundary cells, L_∞ norm of wall pressure errors is equal to that of global pressure errors. For simplicity, only L_2 norm of wall pressure errors is given.

From the results shown in Fig. 36, the L_2 norm of wall pressure errors obtained by G-stencil ($p = 0$) is lower than

Table 7. Global pressure errors and average stencil size of different stencils on the vfin grid.

Different stencils	L_2 norm of global pressure errors	L_∞ norm of global pressure errors	Average stencil size
V-stencil	0.000109909	0.000631396	11.8339
F-stencil	0.000066257	0.000612726	8.896
G-stencil ($p = 0$)	0.0000541208	0.000457848	6.9375
G-stencil ($p = 1$)	0.0000454133	0.000366076	6.9375
G-stencil ($p = 2$)	0.0000427758	0.000331916	6.9375

(2) AR ≈ 8

As shown in Figs. 37 and 39, with the increase of cell aspect ratio, the results demonstrate the same trends as the case of AR ≈ 2.5. From Fig. 38, it can be easily found that with the increase of parameter p, the grid skewness is dramatically reduced. For the computational results, both global and wall pressure errors of the improved global-direction stencil are the lowest among all methods we tested. Hence, on the high-aspect-ratio triangular grid, this improved method is also well performed.
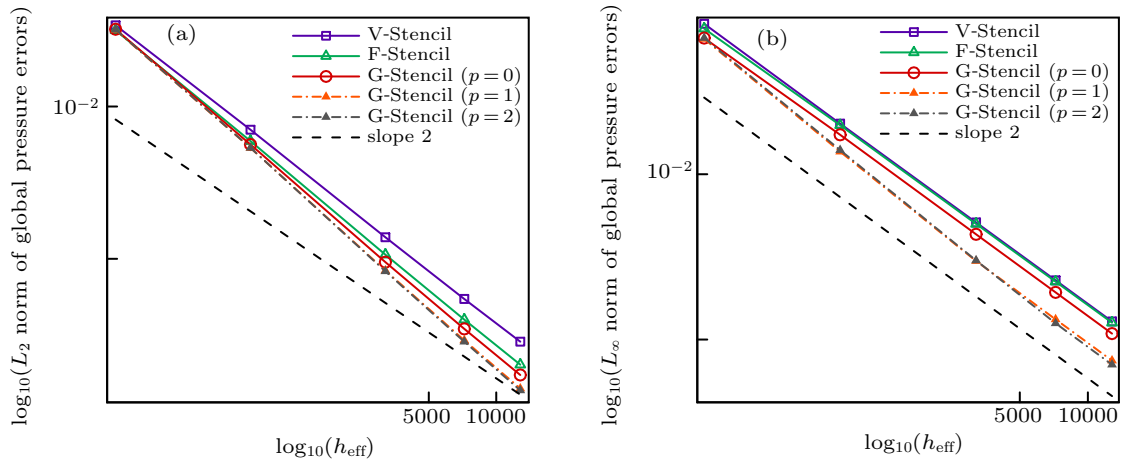
Fig. 37. L_2 and L_∞ norms of global pressure errors, and the aspect ratio AR $\approx$ 8: (a) L_2 norm, (b) L_∞ norm.
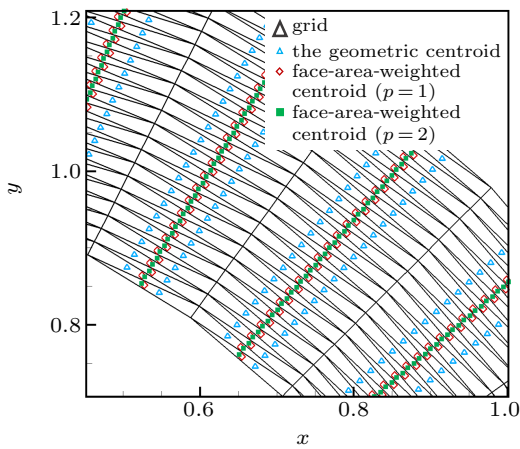

Fig. 38. The geometric centroid and face-area-weighted centroid of grid cells and the aspect ratio AR $\approx$ 8.
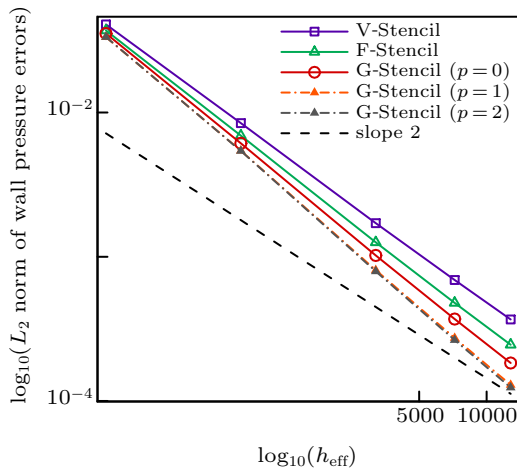

Fig. 39. L_2 norm of wall pressure errors and the aspect ratio AR $\approx$ 8.

4.3.2. Computational results on randomly perturbed triangular grids.

For randomly perturbed grids, the cases of aspect ratio AR $\approx$ 2.5, 4 and 8 are tested, and the errors exhibit a similar trend. For simplicity, here the results of AR $\approx$ 4 are given.

It can be seen from Figs. 40–42 and Table 8 that, when the grid is randomly perturbed, the G-stencil($p = 0$) is superior to V-stecnil and F-stencil on both computational accuracy and efficiency.

For the improved global-direction stencil, from Fig. 41, we find that, although the grid is randomly perturbed, the grid skewness can be effectively reduced by introducing the face-area-weighted centroid. Combining the computational results shown in Table 8, Figs. 40 and 42, we can find that both global and wall pressure errors of the improved global-direction stencil are the lowest among five different stencils.
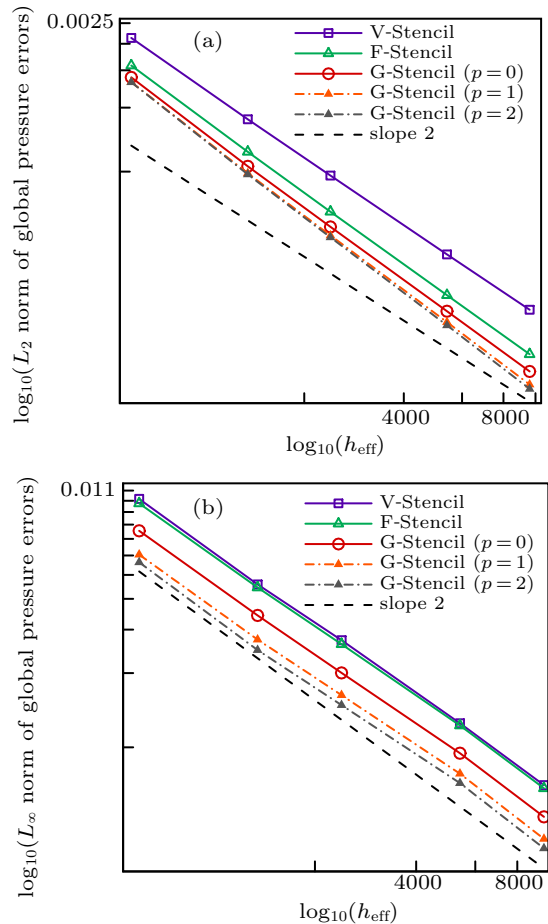

Fig. 40. L_2 and L_∞ norms of global pressure errors on randomly perturbed grids, and the aspect ratio AR $\approx$ 4: (a) L_2 norm, (b) L_∞ norm.
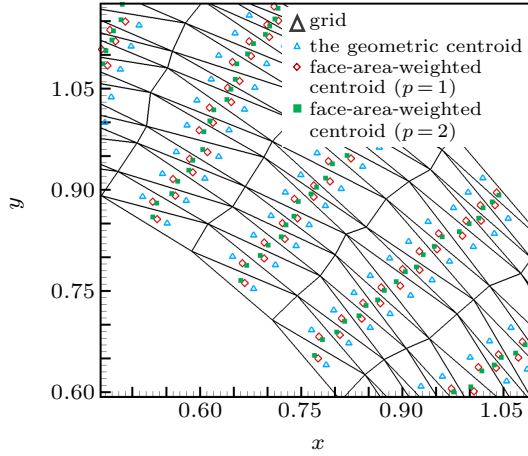
Fig. 41. The geometric centroid and face-area-weighted centroid of grid cells, and the aspect ratio AR ≈ 4.
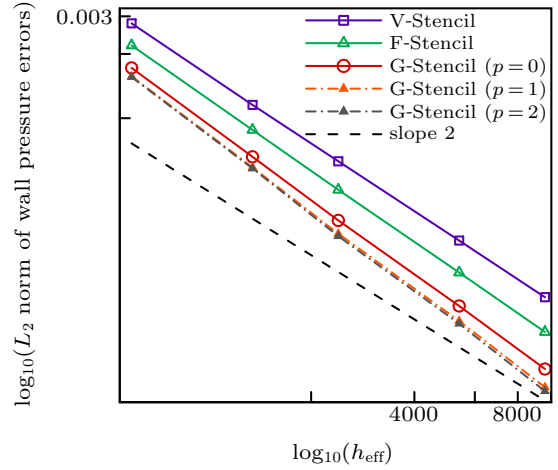

Fig. 42. L_2 norm of wall pressure errors on randomly perturbed triangular grids, and the aspect ratio AR ≈ 4.

Table 8. Global pressure errors of different stencils on the randomly perturbed vfin grid.

Different stencils	L_2 norm of global pressure errors	L_∞ norm of global pressure errors	Average stencil size
V-stencil	0.000261469	0.00144312	11.8008
F-stencil	0.00017859	0.00141231	8.87531
G-stencil ($p = 0$)	0.000151624	0.00112674	6.925
G-stencil ($p = 1$)	0.000128455	0.00085544	6.925
G-stencil ($p = 2$)	0.00012346	0.000787497	6.925

To sum up, combining the computational results on grids with three different aspect ratios, we can fully explain the effectiveness of the improved global-direction stencil. For this numerical example, variation of the flow field is along the radial direction. Based on the global-direction stencil cells, once the face-area-weighted centroid is employed, connections of face-area-weighted centroids are along the radial direction, and consistent with variation of the flow field. Furthermore, both computational accuracy and efficiency of the improved global-direction stencil are always superior to the commonly used V-stencil and F-stencil, as well as the unimproved global-direction stencil.

4.4. Double mach reflection of strong shock waves

From Section 4.1 to Section 4.3, it has been proved that with the employment of "face-area-weighted centroid" on global-direction stencil cells, computational errors could be effectively reduced, and when parameter p is equal to 2, the minimum values of both L_2 and L_∞ errors are achieved. In order to adequately test the numerical performance, such as stability of the improved global-direction stencil on high-mach-number flows, in this section, the double mach reflection of strong shock waves is employed.

This test case is governed by 2-D Euler equations in the domain $x \in [0, 4]$, $y \in [0, 1]$, with an $M_{\text{inf}} = 10$ shock wave inclined at $60°$ with respect to the x-axis, and propagating to the right. The initialization and imposition approach of different boundary conditions could be found in Ref. [36], and are given as follows:

$$\underline{v_0}(x, y) = \begin{cases} \underline{v_A} := \left[8, \ 8.25\cos\dfrac{\pi}{6}, \ -8.25\sin\dfrac{\pi}{6}, \ 116.5\right]^{\text{T}}, & x \leqslant \dfrac{1}{6} + \dfrac{1}{\tan \pi/3}, \\[2ex] \underline{v_B} = [1.4, \ 0, \ 0, \ 1]^{\text{T}}, & x > \dfrac{1}{6} + \dfrac{1}{\tan \pi/3}, \end{cases} \tag{31}$$

where $\underline{v_A}$ is the state traveling behind the right-moving shock wave, and the corresponding boundary conditions could be implemented as

$$\begin{cases} \underline{v}(x=0,\, y,\, t) = \underline{v_A}, & \forall t,\, y \\ \partial_x \underline{v}(x=4,\, y,\, t) = 0, & \forall t,\, y \\ \underline{v}(0 \leqslant x \leqslant x_{sw_u}(t),\, y=1,\, t) = \underline{v_A}, & \forall t \\ \underline{v}(x_{sw_u}(t) < x \leqslant 4,\, y=1,\, t) = \underline{v_B}, & \forall t \\ \underline{v}\left(0 \leqslant x \leqslant \dfrac{1}{6},\, y=0,\, t\right) = \underline{v_A}, & \forall t \\ \begin{bmatrix} \partial_y \rho \\ \partial_y u \\ v \\ \partial_y p \end{bmatrix}\left(\dfrac{1}{6} < x \leqslant 4,\, y=0,\, t\right) = \begin{bmatrix} 0 \\ 0 \\ 0 \\ 0 \end{bmatrix}, & \forall t \end{cases} \quad (32)$$

where $x_{sw_u}(t)$ is the practical location of right-moving shock wave at upper boundary, and can be formulated as

$$\begin{cases} x_{sw_u}(t) = \dfrac{1}{6} + \dfrac{1}{\tan(\pi/3)} + S_{sw_x} t, \\ S_{sw_x} = \dfrac{10}{\sin(\pi/3)}. \end{cases} \quad (33)$$

Table 9. Cell aspect ratio and distribution of background quadrilateral grids in x and y directions.

Different grids	Distribution in x and y directions	Aspect ratio (AR)
Grid 1	160×100	2.5
Grid 2	180×240	5.3
Grid 3	90×190	8.4
Grid 4	100×280	11.2

Four sets of triangular grids with different aspect ratios are generated by splitting quadrilateral grids with right diagonals, and the distributions as well as the corresponding aspect ratios are listed in Table 9.

For simplicity, flow fields of V-stencil, F-stencil, G-stencil ($p=0$) and G-stencil ($p=2$) at $t=0.2$ on grids with AR = 2.5, 5.3 and 11.2 are shown as follows: (1) AR = 2.5 ($t=0.2$). (2) AR = 5.3 ($t=0.2$).

From Figs. 43 and 44, we can easily find that, when the grid is not highly anosotropic, stable numerical performances are exhibited on all stencils we tested. However, with the increasing cell aspect ratio, divergent computing caused by instability first appears on face-neighbor stencil, while other three stencils are well performed. On this basis, we continue to increase the cell aspect ratio. As demonstrated in Fig. 45, when AR equals 11.2, the same instability occurs on vertex-neighbor stencil as well. Nevertheless, both unimproved and improved global-direction stencils with $p=0$ and $p=2$ are always stable, and reflections of shock waves are well displayed.

As a result, in high-mach-number flow, the global-direction stencil and its improvement have a more stable numerical performance than commonly used vertex-neigbor and face-neighbor stencils. What's more, the effectiveness as well as superiorities of the improved global-direction stencil are verified.
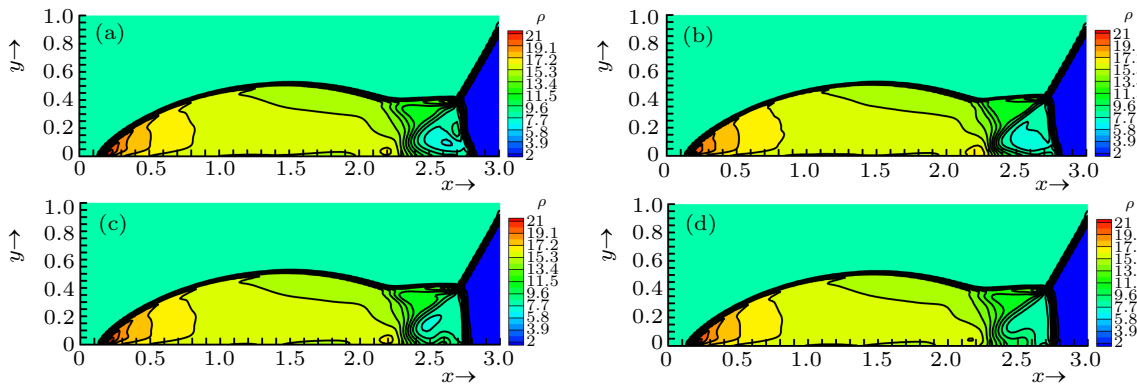

Fig. 43. Flow fields of four different stencils with AR = 2.5 and $t=0.2$: (a) V-stencil, (b) F-stencil, (c) G-stencil ($p=0$), (d) G-stencil ($p=2$).
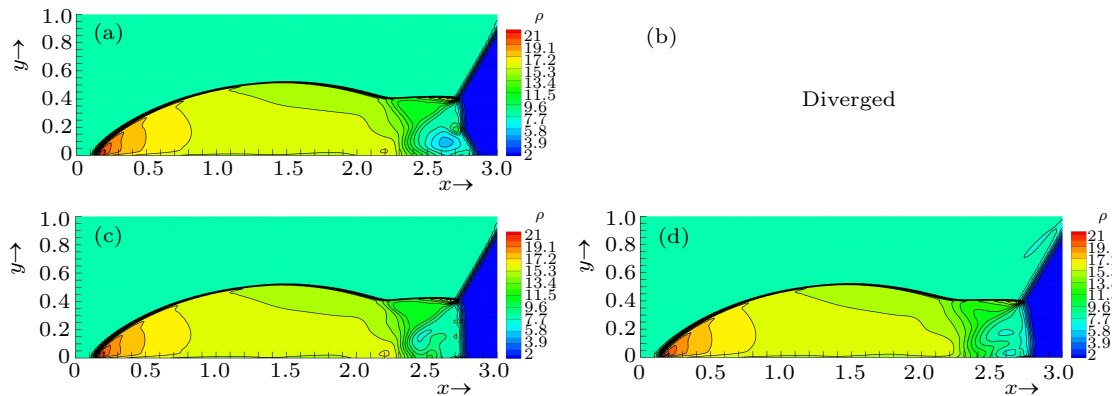

Fig. 44. Flow fields of four different stencils with AR = 5.3 and $t=0.2$, where "Diverged" in red represents the divergent computing. (a) V-stencil. (b) F-stencil. (c) G-stencil ($p=0$). (d) G-stencil ($p=2$).

Fig. 45. Flow fields of four different stencils with AR = 11.2 and $t = 0.2$, where "Diverged" in red represents the divergent computing. (a) V-stencil. (b) F-stencil. (c) G-stencil ($p = 0$). (d) G-stencil ($p = 2$).
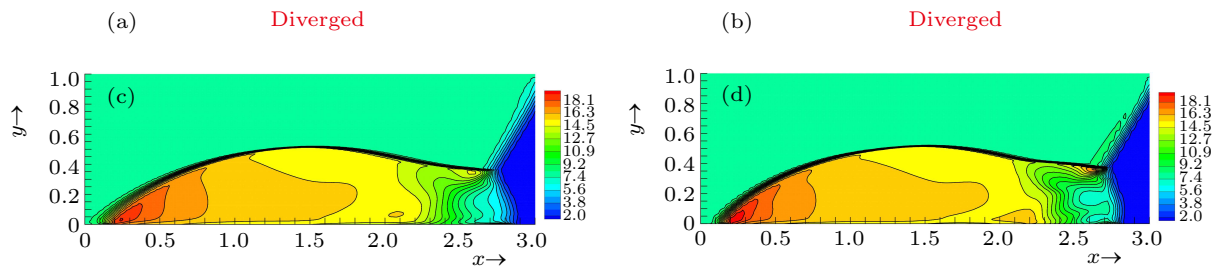
5. Conclusion and future work

In summary, we have realized that, although global direction stencil cells are along the normal and tangential directions of the wall, the only data required for the gradient reconstruction are flow variables evaluated at the reference point rather than stencil cells themselves. Hence, it is hard to reply whether the variation of flow field can be effectively captured or not, especially for high-aspect-ratio triangular grids. If we still choose the reference point at the geometric centroid, the connection of reference points along the boundary normal direction will be obviously skewed. Therefore, in order to obtain a better reflection of the flow-field characteristics, the location of reference point within stencil cells is more decisive.

Inspired by an approach to reduce the grid skewness, where the face-area-weighted centroid[20] is utilized to replace the geometric centroid, and with the increase of parameter p, the grid skewness is gradually eliminated, and the line connecting face-area-weighted centroids are almost parallel to the normal direction of the wall. On this basis, the global-direction stencil is improved by the employment of face-area-weighted centroid on high-aspect-ratio triangular grids, to realize the grid skewness reduction and a more accurate reflection of the flow-field characteristics. Since the position of the reference point has been changed, the finite volume method from a differential form is utilized.

For the computational results, the second-order accuracy with the point solution and the source term vectors in evaluation have been demonstrated by three steady numerical examples, that is, errors of the improved global-direction stencil are remarkably lower than those of vertex-neighbor and face-neighbor stencils, as well as the unimproved global-direction stencil in all steady numerical examples we tested. In double mach reflection of strong shock waves, both unimproved and improved global-direction stencil are always stable, while vertex-neighbor and face-neighbor stencils bring about the divergent computing on high-aspect-ratio triangular grids. What's more, during the gradient reconstruction, this novel stencil requires fewer stencil cells than two com-

monly used stencils. Therefore, both computational accuracy and stability as well as efficiency are greatly improved, and the superiority of this improvement is verified.

In future work, we will continue to extend the improved global-direction stencil on high-order unstructured finite volume methods. Because the numerical cases utilized in this study are boundary-layer-type and simple-shape flows, further investigations of improved global-direction stencils for parallel computing, as well as practical viscous and turbulent flows with complex surface are essential to examine their effectiveness. In addition, to improve the generality of this novel method and to simplify the implementation process, approach of using different stencils at different local fields is also necessary to test its feasibility.

References

[1] Mavriplis D J 1997 *Annu. Rev. Fluid. Mech.* **29** 473
[2] Qin J X, Chen Y M and Deng X G 2019 *Chin. Phys. B* **28** 104701
[3] Venkatakrishnan V 1996 *AIAA J.* **34** 533
[4] Diskin B and Thomas J L 2011 *AIAA J.* **49** 836
[5] Diskin B, Thomas J L, Nielsen E J, Nishikawa H and White J A 2010 *AIAA J.* **48** 1326
[6] Fu Z and Liu K X 2012 *Chin. Phys. B* **21** 040202
[7] Sozer E, Brehm C and Kiris C C 2014 *Proceedings of the 52nd Aerospace Sciences Meeting*, January 13–17, 2014 Convention Center, Washington DC, p. 1440
[8] Jameson A and Mavriplis D J 1986 *AIAA J.* **24** 611
[9] Mavriplis D J 1988 *AIAA J.* **26** 824
[10] Zhou Y F and Feng X S 2012 *Chin. Phys. Lett.* **29** 094703
[11] Xiong M, Deng X G, Gao X, Dong Y D, Xu C F and Wang Z H 2018 *Comput. Fluids* **172** 426
[12] Veluri S P, Roy C J and Luke E A 2012 *Comput. Fluids* **70** 59
[13] Ghoreyshi M, Seidel J, Bergeron K, Jirasek A, Lofthouse A J and Cummings R M 2015 *Proceedings of the 53rd Aerospace Sciences Meeting*, January 5–9, 2015 Kissimmee, Florida, p. 407
[14] Kallinderis Y and Fotia S 2015 *J. Comput. Phys.* **280** 465
[15] Dannenhoffer J 2012 *Proceedings of the 50th Computational Fluid Dynamics Conference*, January 9–12, 2012 Nashville, Tennessee, p. 610
[16] Braaten M and Shyy W 1986 *Numer. Heat Transfer B: Fundamentals* **9** 559
[17] Denner F, Wachem V and Berend G M 2015 *J. Comput. Phys.* **298** 466
[18] Zangeneh R and Ollivier-Gooch C F 2017 *Comput. Fluids.* **156** 590
[19] Veluri S P 2010 *Code verification and numerical accuracy assessment for finite volume CFD codes* (Ph.D. Dissertation) (Blacksburg: Virginia Polytechnic Institute and State University)
[20] Nishikawa H 2020 *J. Comput. Phys.* **401** 109001

[21] Diskin B and Thomas J L 2007 *NIA Report: Accuracy analysis for mixed-element finite-volume discretization schemes*

[22] Barth T 1993 *Proceedings of the 31st Aerospace Sciences Meeting*, January 11–14, 1993 Reno, Nevada, p. 668

[23] Ollivier-Gooch C F and Altena M V 2002 *J. Comput. Phys.* **181** 729

[24] Sejekan C B and Ollivier-Gooch C F 2016 *Comput. Fluids* **139** 216

[25] Loseille A, Dervieux A and Alauzet F 2010 *J. Comput. Phys.* **229** 2866

[26] Toro E 1999 *Riemann Solvers and Numerical Method for Fluid Dynamics - A Practical Introduction* (Berlin: Springer) p. 2

[27] Barth T and Jespersen D 1989 *Proceedings of the 27th Aerospace Sciences Meeting*, January 8–12, 1989 Reno, Nevada, p. 366

[28] Roe P L 1986 *Annu. Rev. Fluid. Mech.* **18** 337

[29] Jalali A and Ollivier-Gooch C F 2017 *Comput. Fluids* **143** 32

[30] Roy C J 2005 *J. Comput. Phys.* **205** 131

[31] Katz A and Sankaran V 2011 *J. Comput. Phys.* **230** 7670

[32] Roache P J 2002 *J. Fluids. Eng.* **124** 4

[33] Park M A, Barral N, Ibanez D, Kamenetskiy D S, Krakos J A, Michal T R and Loseille A 2018 *Proceedings of the 56th AIAA Aerospace Sciences Meeting*, January 8–10, 2018 Kissimmee, Florida, p. 1103

[34] Dong Y D, Deng X G, Gao X, Xiong M and Wang G X 2018 *Comput. Fluids* **172** 284

[35] Krivodonova L and Berger M 2006 *J. Comput. Phys.* **211** 492

[36] Gerolymos L, Senechal M and Vallet I 2009 *J. Comput. Phys.* **228** 8481